

University of Groningen

## Radial gas motions in The H I Nearby Galaxy Survey (THINGS)

Schmidt, Tobias M.; Bigiel, Frank; Klessen, Ralf S.; de Blok, W. J. G.

*Published in:*  
Monthly Notices of the Royal Astronomical Society

*DOI:*  
[10.1093/mnras/stw011](https://doi.org/10.1093/mnras/stw011)

**IMPORTANT NOTE:** You are advised to consult the publisher's version (publisher's PDF) if you wish to cite from it. Please check the document version below.

*Document Version*  
Publisher's PDF, also known as Version of record

*Publication date:*  
2016

[Link to publication in University of Groningen/UMCG research database](#)

*Citation for published version (APA):*

Schmidt, T. M., Bigiel, F., Klessen, R. S., & de Blok, W. J. G. (2016). Radial gas motions in The H I Nearby Galaxy Survey (THINGS). *Monthly Notices of the Royal Astronomical Society*, 457(3), 2642-2664.  
<https://doi.org/10.1093/mnras/stw011>

**Copyright**

Other than for strictly personal use, it is not permitted to download or to forward/distribute the text or part of it without the consent of the author(s) and/or copyright holder(s), unless the work is under an open content license (like Creative Commons).

The publication may also be distributed here under the terms of Article 25fa of the Dutch Copyright Act, indicated by the "Taverne" license. More information can be found on the University of Groningen website: <https://www.rug.nl/library/open-access/self-archiving-pure/taverne-amendment>.

**Take-down policy**

If you believe that this document breaches copyright please contact us providing details, and we will remove access to the work immediately and investigate your claim.

*Downloaded from the University of Groningen/UMCG research database (Pure): <http://www.rug.nl/research/portal>. For technical reasons the number of authors shown on this cover page is limited to 10 maximum.*

# Radial gas motions in The H I Nearby Galaxy Survey (THINGS)

Tobias M. Schmidt,<sup>1,2★</sup> Frank Bigiel,<sup>1</sup> Ralf S. Klessen<sup>1,3,4</sup> and W. J. G. de Blok<sup>5,6,7</sup>

<sup>1</sup>*Institut für Theoretische Astrophysik, Zentrum für Astronomie, Universität Heidelberg, Albert-Ueberle Str. 2, D-69120 Heidelberg, Germany*

<sup>2</sup>*Max-Planck-Institut für Astronomie, Königstuhl 17, D-69117 Heidelberg, Germany*

<sup>3</sup>*Kavli Institute for Particle Astrophysics and Cosmology, Stanford University, SLAC National Accelerator Laboratory, Menlo Park, CA 94025, USA*

<sup>4</sup>*Department of Astronomy and Astrophysics, University of California, 1156 High Street, Santa Cruz, CA 95064, USA*

<sup>5</sup>*Netherlands Institute for Radio Astronomy (ASTRON), Postbus 2, NL-7990 AA Dwingeloo, the Netherlands*

<sup>6</sup>*Astrophysics, Cosmology and Gravity Centre, Department of Astronomy, University of Cape Town, Private Bag X3, Rondebosch 7701, South Africa*

<sup>7</sup>*Kapteyn Astronomical Institute, University of Groningen, PO Box 800, NL-9700 AV Groningen, the Netherlands*

Accepted 2015 December 28. Received 2015 December 7; in original form 2015 April 9

## ABSTRACT

The study of 21 cm line observations of atomic hydrogen allows detailed insight into the kinematics of spiral galaxies. We use sensitive high-resolution Very Large Array data from The H I Nearby Galaxy Survey (THINGS) to search for radial gas flows primarily in the outer parts (up to  $3 \times r_{25}$ ) of 10 nearby spiral galaxies. Inflows are expected to replenish the gas reservoir and fuel star formation under the assumption that galaxies evolve approximately in steady state. We carry out a detailed investigation of existing tilted ring fitting schemes and discover systematics that can hamper their ability to detect signatures of radial flows. We develop a new Fourier decomposition scheme that fits for rotational and radial velocities and simultaneously determines position angle and inclination as a function of radius. Using synthetic velocity fields we show that our novel fitting scheme is less prone to such systematic errors and that it is well suited to detect radial inflows in discs. We apply our fitting scheme to 10 THINGS galaxies and find clear indications of, at least partly previously unidentified, radial gas flows, in particular for NGC 2403 and NGC 3198 and to a lesser degree for NGC 7331, NGC 2903 and NGC 6946. The mass flow rates are of the same order but usually larger than the star formation rates. At least for these galaxies a scenario in which continuous mass accretion feeds star formation seems plausible. The other galaxies show a more complicated picture with either no clear inflow, outward motions or complex kinematic signatures.

**Key words:** galaxies: kinematics and dynamics – galaxies: structure – radio lines: galaxies.

## 1 INTRODUCTION

The question of how spiral galaxies manage to sustain star formation activity over cosmological times is key to our understanding of galaxy formation and evolution. Finding an answer is not easy, given that most observations point towards very short gas depletion time-scales. For example, our Galaxy forms new stars at a rate of  $2\text{--}4\text{ M}_\odot\text{ yr}^{-1}$  (Naab & Ostriker 2006; Adams et al. 2013). Its gas mass is about  $8 \times 10^9\text{ M}_\odot$  (see Ferrière 2001 and Kalberla 2003). If we assume a constant star formation rate (SFR; Binney, Dehnen & Bertelli 2000), then the remaining gas should be converted into stars within about 2–4 Gyr. Similar values or of the order of only a few billion years are reported for many nearby disc galaxies (for observational evidence, see for example Bigiel et al. 2008, Leroy et al. 2008, or Bigiel et al. 2011; for theoretical arguments, see e.g. Pflamm-Altenburg & Kroupa 2009). At higher redshifts of  $z \approx 2$ , the depletion time-scale can be even shorter. Values of 0.6–1.5 Gyr

have been inferred for the total gas (e.g. Genzel et al. 2010), while the numbers for the molecular gas component can be as low as 0.5 Gyr (Daddi et al. 2010). In vigorously star-forming merging systems, the observations suggest even shorter time-scales, down to 0.1 Gyr.

We note, however, that these are average numbers, with the data showing significant variations, both from galaxy to galaxy and within each galaxy as a function of many parameters, not just column density (for further discussions, see e.g. Saintonge et al. 2011, 2012; Leroy et al. 2013; Shetty, Kelly & Bigiel 2013; Shetty et al. 2014a; Shetty, Clark & Klessen 2014b).

If we discard the possibility that most spiral galaxies are observed at the verge of running out of gas, and instead assume that they evolve in quasi-steady state, then this requires a supply of fresh gas delivered to the galaxy at a rate roughly equal to its SFR. Indeed, there is additional support for this picture.

First, galactic accretion flows are a natural outcome of cosmological structure formation calculations. For example, Dekel et al. (2009) and Ceverino, Dekel & Bournaud (2010) argue that massive galaxies are continuously fed by steady, narrow, cold gas streams

\* E-mail: tschmidt@mpia-hd.mpg.de

that penetrate through the accretion shock at the virial radius into the central galaxy (see also Marinacci, Pakmor & Springel 2014). Roughly three quarters of all galaxies forming stars at a given rate are fed by smooth streams (see also Agertz, Teyssier & Moore 2009), at least up to redshifts of  $z \approx 2$ . The details of this process are still under debate, as they seem to depend on the numerical method employed and on the way gas cooling is implemented (e.g. Bird et al. 2013). Nevertheless, even if most of the gas shocks at the virial radius and builds up a hot ionized halo, some fraction of it may cool down again and become available for disc accretion. As proposed by Peek (2009) this gas could condense into higher density clumps at the interface between halo and disc and then ‘rain’ down on to the disc later in the process. This transport of matter converts potential energy into kinetic energy, and constitutes a source for the observed turbulence on smaller scales and thus contributes to controlling the star formation process in the galaxy (Mac Low & Klessen 2004). Indeed, gas accretion has been proposed to be the main source of turbulence in the extended outer disc of galaxies, where the star formation activity is low and consequently stellar feedback cannot provide enough energy and momentum to explain the observed velocity dispersion in the H I gas (Klessen & Hennebelle 2010).

Secondly, indirect support for continuous accretion comes from the fact that the observed amount of atomic gas in the Universe appears to be roughly constant, from a redshift of  $z \approx 3$  till today, while the stellar content continues to increase, suggesting that overall the H I content of typical galaxies is continuously replenished from some external reservoir (Hopkins, McClure-Griffiths & Gaensler 2008; Prochaska & Wolfe 2009).

Thirdly, for our Galaxy at least, further evidence for an ongoing inflow of low-metallicity material stems from the presence of deuterium in the solar neighbourhood (Linsky 2003) as well as in the Galactic Centre (Lubowich et al. 2000). As deuterium is destroyed in stars and as there is no other known source of deuterium in the Milky Way, it is thought to be pristine material of extragalactic origin (Ostriker & Tinsley 1975; Chiappini, Renda & Matteucci 2002) falling on the Galaxy for the first time.

If gas is accreted on to a disc galaxy from great distances, the new material is most likely delivered to large galactic radii. This is a consequence of angular momentum conservation, and it finds additional support from the fact that the outer disc simply has a larger cross-section than the central regions. As most of the star formation occurs in the inner parts, one might expect an inward flow of gas through the disc. It is this radial mass flux that we aim to detect in this study.

In many galaxies, neutral hydrogen (H I) is found out to radii much larger than the optical disc (e.g. Walter et al. 2008; Bigiel et al. 2010a,b). This gas provides us with the possibility to look for infall signatures. Indeed, the asymmetry commonly seen in the outer discs of galaxies is often considered to be the result of gas accretion (Ostriker & Binney 1989; Jiang & Binney 1999; Bournaud et al. 2005; Fraternali & Binney 2008), triggered either by recent minor mergers (Zaritsky & Rix 1997) or by tidal interaction (Kornreich, Lovelace & Haynes 2002). Some galaxies show one very prominent spiral arm extending beyond the rest of the H I disc. Others have tails or a very asymmetric and lopsided disc or show substantial warps, especially in the outskirts. Also H I bridges to companion galaxies are observed. Sancisi et al. (2008) argue that these observations are evidence for recent or ongoing accretion and infall of cold gas, and they claim that in at least 25 per cent of field galaxies indications for a merger event or tidal interactions can be detected.

The detection of high-velocity clouds (HVCs; Miller, Bregman & Wakker 2009) points in a similar direction. These are extraplanar H I clouds with low metallicities (van Woerden & Wakker 2004), with anomalous kinematics (Fraternali et al. 2002), and with velocity gradients that are perpendicular to the Galactic plane (Fraternali et al. 2005). Many of them have a ‘head–tail’ shape as is expected for the motion of colder and denser clouds through the tenuous hot halo gas of the Milky Way. Their origin, however, remains unclear. They could be fresh material falling on to the Galaxy for the first time. Or the HVCs could be the fallback of Galactic fountain flows (Shapiro & Field 1976; Bregman 1980). In this case, HVCs contain enriched gas that is ejected from the disc by stellar feedback. This gas is likely to fall back at larger radii. As it is lifted from the disc mid-plane, it runs down a vertical pressure gradient and some fraction of it spreads to larger radii. It travels through the hot halo gas above the plane that is rotating more slowly (Fraternali & Binney 2006, 2008). As a consequence, the ejected material has larger angular momentum than its environment, and as it mixes with the extraplanar gas, it falls back to the disc at larger radii than it came from.

Gas that accretes on to the outer disc must move inwards through this disc, before it becomes converted into stars in the star-forming inner regions of the galaxy. To search for these radial gas flows, Wong, Blitz & Bosma (2004) studied seven spiral galaxies based on CO and H I observations. They found elliptical and bar streaming motions and could give upper limits on the magnitude of possible radial inflows. However, without the availability of deep large-scale maps, the focus was on the inner discs, where the non-circular motions detected were of the order of  $5\text{--}10\text{ km s}^{-1}$ , comparable to the level of turbulence in the disc. Our approach is different. We focus on the extended outer discs of nearby spiral galaxies, where the gas density is low and therefore the local streaming velocity needs to be high in order to result in an appreciable mass flow.

We base our analysis on 21 cm line observations of neutral hydrogen in The H I Nearby Galaxy Survey (THINGS; Walter et al. 2008). This allows us to trace gas up to very large radii, typically far beyond the optical radius of the galaxy. The survey provides two-dimensional high-resolution velocity maps, and our approach to model these velocity fields is in general known as ‘tilted ring fit’. The map is decomposed into individual rings which are circular within the plane of the disc, but inclined with respect to the line of sight and therefore appear elliptical. For each of them, inclination, position angle, circular velocity and other parameters are determined. The method was first described by Rogstad, Lockhart & Wright (1974) and developed further by e.g. Bosma (1978) and Begeman (1987). These studies derived rotation curves for a number of galaxies based on H I maps from the Westerbork Synthesis Radio Telescope. Other studies extended this concept by also fitting non-circular velocity components of different kinds to the velocity field.

High-order harmonic decompositions were used by Schoenmakers, Franx & de Zeeuw (1997, applied to H I observations of NGC 2403 and NGC 3198) and Trachternach et al. (2008, search for elongated potential in 19 THINGS galaxies). Kinematic studies assuming flat discs and models of particular streaming motions were conducted by Wong et al. (2004, search for radial inflow based on CO and H I observations of seven spiral galaxies), Spekkens & Sellwood (2007, bar-like streaming motions in NGC 2976 based on H $\alpha$  and CO observations; development of the VELFIT code<sup>1</sup>) and Sellwood & Sanchez (2010, improvement

<sup>1</sup> <http://www.physics.rutgers.edu/~spekkens/velfit/>

**Table 1.** Properties of galaxies analysed.

Name	Type	RA ( $^{\circ}$ )	Dec. ( $^{\circ}$ )	Distance (Mpc)	$r_{25}$ (arcmin)	$r_{25}$ (kpc)	$M_{\text{H I}}$ ( $10^8 M_{\odot}$ )	SFR ( $M_{\odot} \text{ yr}^{-1}$ )	$\Gamma_{\text{H I}}(r > r_{25})$ ( $M_{\odot} \text{ yr}^{-1}$ )
NGC 2403	SBcd	114.2129	65.6008	3.2	7.92	7.38	25.8	0.38	$-1.20 \pm 0.1$
NGC 2841	Sb	140.5108	50.9764	14.1	3.46	14.19	85.8	0.74	$0.36 \pm 0.5$
NGC 2903	SBbc	143.0421	21.5011	8.9	5.87	15.21	43.5	0.44	$-0.54 \pm 0.1$
NGC 3198	SBc	154.9792	45.5497	13.8	3.23	12.96	101.7	0.93	$-1.02 \pm 0.1$
NGC 3521	SBbc	166.4525	-0.0358	10.7	4.16	12.94	80.2	2.10	$-0.91 \pm 0.8$
NGC 3621	Sd	169.5688	-32.8142	6.6	4.89	9.38	70.7	2.09	$0.59 \pm 0.9$
NGC 5055	Sbc	198.9550	42.0292	10.1	5.87	17.26	91.0	2.12	$1.35 \pm 0.5$
NGC 6946	SBcd	308.7175	60.1539	5.9	5.74	9.85	41.5	3.24	$-13.12 \pm 2.0$
NGC 7331	SAb	339.2671	34.4158	14.7	4.56	19.50	91.3	2.99	$-1.03 \pm 0.7$
NGC 0925	SBd	36.8187	33.5789	9.2	5.36	14.34	45.8	0.56	$2.47 \pm 0.5$

Coordinates, types, distances,  $r_{25}$  (the radius where the galaxy  $B$ -band surface brightness drops below 25 mag arcsec $^{-2}$ ) and H I masses as measured by THINGS are from Walter et al. (2008), SFR are from Leroy et al. (2008), except for NGC 2903 (Popping, Perez & Zurita 2010) and NGC 3621 (Walter et al. 2008). The last column gives our measurement of the average radial mass flow rate outside of  $r_{25}$ . Negative values denote inflow, positive outflow. The given uncertainties are the average errors of the radial H I mass flow outside of  $r_{25}$ .

and extension of the previous study to five other galaxies based on H $\alpha$  and H I measurements). Spekkens and collaborators later developed DISKFIT (Sellwood & Spekkens 2015),<sup>2</sup> an improved version of VELFIT which is not strictly limited to constant inclination and can also operate on photometric data. Kuzio de Naray et al. (2012) applied DISKFIT to H $\alpha$ , CO and H I kinematic data of NGC 6503.

Models with constant inclination are not suitable for studies including the regime beyond the star-forming disc, where the H I discs often show variable inclination. Furthermore, high-order Fourier decompositions would require the disc geometry to be determined in a separate, prior step by a low-order tilted ring fit. In this study, we develop a fitting scheme that circumvents the complications associated with this two-step approach and at the same time can be applied to discs with (moderately) varying inclinations.

Our study is organized as follows. In Section 2, we describe the THINGS data set. In Section 3, we outline our new method, discuss its stability properties and compare to previous approaches. In Section 4, we apply our method to mock data, investigate its stability properties and discuss its limitations. We apply the method to a sample of 10 galaxies from the THINGS survey and present our results in Section 5. Finally, we summarize and conclude in Section 6.

## 2 DATA

The main observational basis of this study is high spatial resolution observations of atomic hydrogen for a large set of nearby galaxies. These are taken from the THINGS survey (Walter et al. 2008<sup>3</sup>). It is a large survey of 34 nearby galaxies in the 21 cm line of neutral hydrogen and was conducted at the NRAO Very Large Array (VLA). The survey provides a high spatial resolution of 6–12 arcsec and a channel width of 5 km s $^{-1}$ .

Not all galaxies targeted within the THINGS survey are suitable for our analysis. Objects have to be well resolved (large angular size), have intermediate inclinations (above 30°–40°) and show a relatively regular velocity field. We applied our method to all promising candidates and in the end, our analysis yielded useful results for 10 galaxies which are listed in Table 1.

Our targets have distances between 3 and 15 Mpc which results in a physical resolution between 100 and 500 pc. The survey provides a detailed census of the H I distribution in a large number of nearby galaxies at high angular resolution as is thus well suited for kinematic studies.

For this work, we use various data products provided by the survey. The intensity (zeroth-moment) maps reflects the total H I column density and the first-moment map the H I velocity field. Data cubes and moment maps are available in two versions. They differ in the weighting scheme applied to the interferometric data from individual antenna pairs during image reconstruction. The ROBUST scheme is optimized for maximizing resolution and contrast by giving long baselines a higher impact. We choose the data products assuming NATURAL weighting. This scheme is more suitable for us since it provides better signal-to-noise (S/N) and better recovers diffuse emission. A detailed description of the survey and the data processing can be found in Walter et al. (2008).

Additionally, we also use velocity maps derived by fitting Hermite functions directly to spectra in THINGS data cubes. They should better reflect the bulk motion of the gas but require data with slightly higher S/N ratio compared to first-moment maps.

There is always the possibility that interferometric observations miss flux at large spatial scales due to incomplete  $uv$ -coverage. To minimize this issue, THINGS includes observations in the compact VLA-D configuration. For verification, we compare the THINGS intensity maps to single-dish observations from the Effelsberg–Bonn H I Survey (EBHIS, Kerp et al. 2011) and find no significant discrepancy in total fluxes for the regions of the discs we model in this study. A more detailed analysis by Daniel Lenz (AIfA, University of Bonn, private communication) came to the similar conclusion that usually no more than 10 per cent flux is missing in the THINGS maps, at least as long as the galaxy fits within the VLA primary beam.

Optical observations are used to find the nearside of our target galaxies which, in combination with the velocity information, allows us to uniquely determine the direction of rotation and to break the degeneracy between inflow and outflow. The optical images are taken from the NASA/IPAC Extragalactic Database (NED).<sup>4</sup> To compare our inflow results to the average recent SFR, we use

<sup>2</sup> <http://www.physics.rutgers.edu/~spekkens/diskfit/>

<sup>3</sup> The H I Nearby Galaxy Survey: <http://www.mpia-hd.mpg.de/THINGS>

<sup>4</sup> <http://ned.ipac.caltech.edu>

*GALEX* far-UV (FUV) images. We use the final data products available from the *GALEX* archive.<sup>5</sup>

### 3 THEORY AND METHOD

In Sections 3.1 and 3.2, we introduce basic theoretical concepts regarding modelling 2D velocity fields of disc galaxies and describe the different fitting procedures we evaluated. Sections 3.3 and 3.4 compare sequential versus simultaneous fitting approaches and their impact on derived quantities. The optimum procedure we finally adopted is described in Section 3.5

#### 3.1 Tilted ring analysis

The quantity accessible to observation is the line-of-sight velocity ( $V_{\text{los}}$ ). To infer the rotational and radial velocities of the gas in the disc from spatially resolved measurements of  $V_{\text{los}}$ , one has to utilize a specific model that can be fitted to the data. The straightforward approach is to assume a velocity field which is symmetric with respect to the disc centre and projected under some viewing geometry. The measured  $V_{\text{los}}$  then has the form

$$V_{\text{los}} = V_{\text{sys}} + V_{\text{rot}} \sin(i) \cos(\theta) + V_{\text{rad}} \sin(i) \sin(\theta). \quad (1)$$

Here  $V_{\text{sys}}$  denotes the systemic velocity of the galaxy with respect to the observer.  $V_{\text{rot}}$  is the rotation velocity and  $V_{\text{rad}}$  is a velocity component in radial direction in the plane of the disc. The other variables are the inclination  $i$  of the disc and the azimuthal angle  $\theta$  which together with the radius  $R$  forms a polar coordinate frame within the plane of the galaxy. The disc is assumed to be thin and no motions perpendicular to the plane of the galaxy are taken into consideration.

All quantities mentioned above can in general be treated as functions of the radius  $R$ . In the analysis, the disc is basically sliced in circular annuli and the above decomposition of  $V_{\text{los}}$  done for each ring individually which leads to the term ‘tilted ring’ analysis.

The line-of-sight velocity is a function of the sky coordinates while the terms on the right-hand side of equation (1) are functions of the coordinates within the plane of the disc. Therefore, one needs a coordinate transformation between sky coordinates ( $X, Y$ ) and the disc coordinates ( $R, \theta$ ). To do this transformation, the geometry of the disc has to be known. It can be described by the centre coordinates ( $X_C, Y_C$ ), the inclination ( $i$ ) and the position angle of the apparent major axis of the disc (PA) as measured in the plane of the sky. One representation of the transformation equations is the following:

$$\cos(\theta) = \frac{-(X - X_C) \sin(\text{PA}) + (Y - Y_C) \cos(\text{PA})}{R}, \quad (2)$$

$$\sin(\theta) = \frac{-(X - X_C) \cos(\text{PA}) - (Y - Y_C) \sin(\text{PA})}{R \cos(i)}. \quad (3)$$

This transformation is not straightforward to solve for  $R$  and  $\theta$  since the parameters  $X_C, Y_C, \text{PA}$  and  $i$  implicitly depend on  $R$ , if one describes the disc as sequence of independent rings with possibly different inclinations, position angles and centre coordinates. In this case, the global transformation from sky coordinates to disc coordinates is in general neither unique nor continuous. This is, because the rings can overlap or gaps between them can appear. The only reason this transformation can be used in practice is that

$i$  and PA usually vary smooth and slowly. Or to be more specific, the analysis has to be restricted to galaxies where this condition is fulfilled.

An illustration of the analysis is given in Fig. 1. It shows the observed H I velocity of NGC 5055 as a ‘spider’ diagram, where the lines denote regions of constant line-of-sight velocity, and in colours it indicates the corresponding tilted ring fits. It is clearly noticeable that NGC 5055 has a warped disc, but we also see how the tilted ring fit adapts to the varying disc geometry and follows the changing inclination and position angle.

Usually, not all parameters are kept free in a fit. In some schemes like the one implemented in *VELFIT* (Spekkens & Sellwood 2007), it is assumed that the disc is flat, and therefore all radii have the same inclination and position angle. In such cases,  $i$  and PA are determined once for the whole galaxy and then kept fixed for each radius. Because we include the outer parts of the discs in our analysis which are often warped to some degree, we allow PA and  $i$  to vary independently for each ring. Only considering average values of  $i$  and PA would not represent the actual geometry of the disc to the necessary precision.

However, leaving all fit parameters (PA,  $i, X_C, Y_C, V_{\text{rot}}, \dots$ ) completely unconstrained often leads to unstable fit results. We therefore choose to keep the ring centres fixed, assuming that all parts of the galaxy rotate around a common centre of mass. This is a good approximation for galaxies that are not subject to strong external perturbations, such as exerted by a massive satellite galaxy. We determine the galaxy centre from the inner, mostly flat part of the disc and enforce this centre coordinates for all rings.

#### 3.2 Fourier decomposition

By including the  $V_{\text{rad}}$  term, the tilted ring fit as described above already includes non-circular motions. Also all parameters especially inclination and position angle can be allowed to vary from ring to ring and therefore with radius. However, the velocity field of each ring is still restricted to rotational symmetry around the ring centre. One can generalize the model by allowing  $V_{\text{rot}}$  and  $V_{\text{rad}}$  to vary with respect to the azimuthal angle  $\theta$ . Again, it is not possible to allow arbitrary functions here, since not enough observables are available to determine them. The usual approach is to expand the azimuthal dependence of  $V_{\text{rot}}$  and  $V_{\text{rad}}$  in a Fourier series and include terms up to a certain order:

$$V_{\text{rad}}(R, \theta) = B_0 + \sum_{k>0} A_k \sin(k\theta) + B_k \cos(k\theta), \quad (4)$$

$$V_{\text{rot}}(R, \theta) = D_0 + \sum_{k>0} C_k \sin(k\theta) + D_k \cos(k\theta). \quad (5)$$

The line-of-sight velocity has to be expanded in the same way, and for notational convenience a factor  $\sin(i)$  is already pulled out of all Fourier parameters:

$$V_{\text{los}}(R, \theta) = V_{\text{sys}} + \sin(i) \left[ c_0 + \sum_{k>0} s_k \sin(k\theta) + c_k \cos(k\theta) \right]. \quad (6)$$

We denote Fourier parameters corresponding to the velocities in the disc frame by capital letters, while the ones referring to the line-of-sight velocity are lower case.

By inserting equations (4) and (5) in equation (1) and comparing with equation (6), one can find relations between the Fourier coefficients of the line-of-sight velocity and the Fourier parameters of

<sup>5</sup> <http://galex.stsci.edu/>



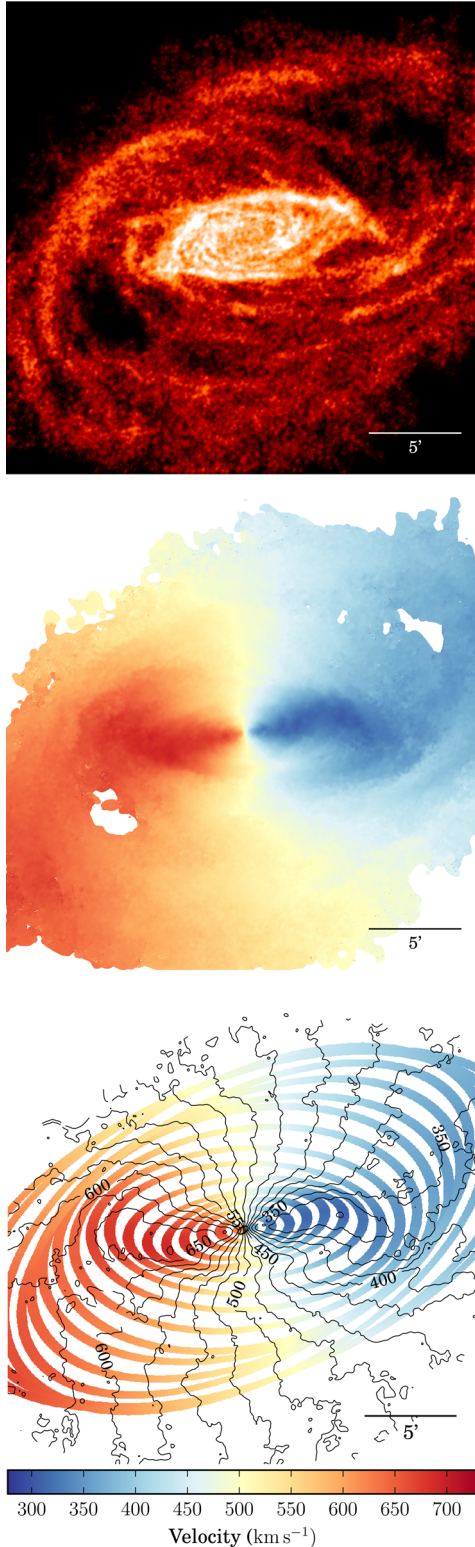


**Figure 1.** Top and centre: zeroth- and first-moment maps of NGC 5055. For the other galaxies, similar images can be found on the THINGS website: <http://www.mpia-hd.mpg.de/THINGS>. Bottom: illustration of a tilted ring fit to the velocity field of NGC 5055. For better visualization only every second ring is shown. The colour scale represents the line-of-sight velocity and overplotted are the THINGS first-moment map velocity contours in steps of  $25 \text{ km s}^{-1}$ .

the velocities in the disc frame:

$$\begin{aligned}
 V_{\text{los}} = V_{\text{sys}} + \frac{1}{2} \sin(i) & \left[ (D_1 + A_1) \right. \\
 & + (2B_0 + C_2 - B_2) \sin(\theta) \\
 & + (2D_0 + D_2 + A_2) \cos(\theta) \\
 & + \sum_{k>1} (C_{k-1} + C_{k+1} + B_{k-1} + B_{k+1}) \sin(k\theta) \\
 & \left. + \sum_{k>1} (D_{k-1} + D_{k+1} - A_{k-1} + A_{k+1}) \cos(k\theta) \right]. \quad (7)
 \end{aligned}$$

One finds that a radial or rotational velocity component of order  $k$  contributes to order  $k - 1$  and  $k + 1$  to the line-of-sight velocity. Also, there are roughly two times as many Fourier coefficients in the disc frame ( $A_k, B_k, C_k, D_k$ ) than are accessible by observations ( $s_k, c_k$ ). This makes a unique reconstruction of the actual velocities impossible.

We therefore restrict our analysis to second order in  $V_{\text{los}}$ , corresponding to first order in  $V_{\text{rot}}$  and  $V_{\text{rad}}$ . This simplifies equation (7) to

$$\begin{aligned}
 V_{\text{los}} = V_{\text{sys}} + \frac{1}{2} \sin(i) & [(D_1 + A_1) \\
 & + (2B_0) \sin(\theta) + (2D_0) \cos(\theta) \\
 & + (C_1 + B_1) \sin(2\theta) + (D_1 - A_1) \cos(2\theta)]. \quad (8)
 \end{aligned}$$

In this simplified model, it is easier to solve for the Fourier coefficients of  $V_{\text{rot}}$  and  $V_{\text{rad}}$ . The comparison to equation (6) shows that the  $V_{\text{los}}$  parameter  $c_1$  directly represents the rotation curve and the  $s_1$  parameter corresponds to the zeroth-order radial velocity, sometimes also denoted as  $V_{\text{rad},0}$ . There are only two remaining degeneracies. In principle, the zeroth-order term  $c_0 = \frac{1}{2}(D_1 + A_1)$  is degenerate with the systemic velocity. However, this is not a significant concern, because the systemic velocity should be the same for all rings and therefore needs to be determined only once. This can, for example, be done by directly using the velocity of the galaxy centre. A degeneracy that cannot be solved concerns  $s_2 = \frac{1}{2}(C_1 + B_1)$ , because  $C_1$  and  $B_1$  only appear in this term. To make progress, we adopt  $C_1 = B_1$ . That is, we assume that both terms contribute equally.

Within a single ring, all parameters are modelled without any radial dependence and therefore with constant rotation velocity. This prohibits a perfect fit to the data in the inner part of a galaxy with roughly linearly rising rotation curve. Because the focus of this study is not the galactic centres, and because spiral galaxies show a mostly flat rotation curve over most of their outer disc, this is not a concern for this study.

Solid-body rotation produces another problem. It leads to parallel isovelocity contours in the observed velocity field and makes it impossible to disentangle  $V_{\text{rot}}$  and  $\sin(i)$ . Therefore, our analysis cannot be applied to dwarf galaxies which usually have linearly rising rotation curves over most of their H I disc. The same effect causes problems in the inner parts of spiral galaxies. Since these parts are not the focus of our study, we disregard this regime when applying our analysis and interpreting our results.

### 3.3 Two-step fit

The Fourier components themselves form an orthogonal base and therefore can be fitted independently of each other. However, at least the components of odd order couple to inclination and position

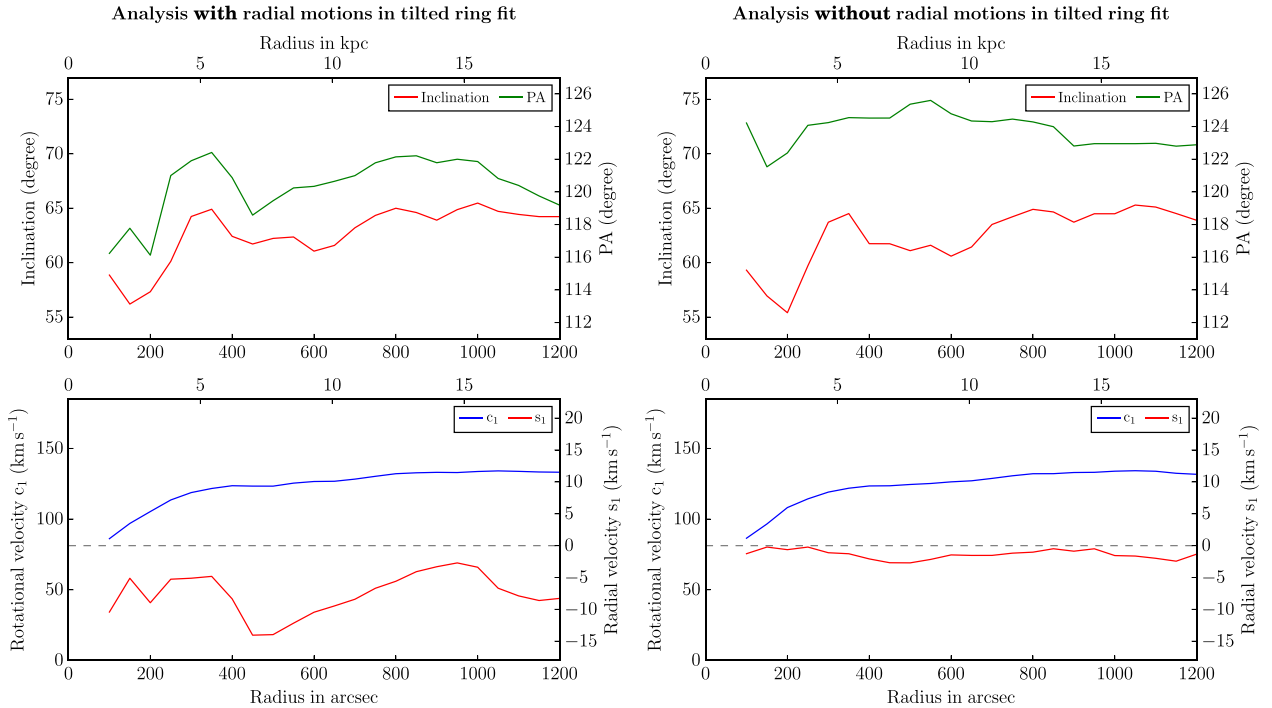


**Figure 2.** Comparison of results obtained by two-step fits to the observed velocity field of NGC 2403, where first the ring geometry is determined in a tilted ring fit and subsequently a Fourier decomposition is performed. Including a radial velocity term already in the tilted ring stage leads to the plots on the left, and omitting such a term leads to the plots on the right. The determined rotation curves and inclinations are similar but the position angle deviates by up to  $6^\circ$  since in the second fit the geometry is optimized according to a model without radial motions. One sees that the position angle adjusts to compensate for radial inflow and thus the following Fourier decomposition is unable to recover a significant radial flow (red line in bottom-right panel). If  $i$ , PA,  $V_{\text{rot}}$  and  $V_{\text{rad}}$  are fitted simultaneously during the tilted ring fit as in the left-hand panels, clear signs for radial motions are obvious (bottom-left panel). Uncertainties are approximately  $\pm 1 \text{ km s}^{-1}$  for  $s_1$  like in Fig. 8.

angle. It is therefore not obvious that one can first determine the ring geometry with a tilted ring fit of low order, and then in a second step, apply a higher order Fourier decomposition using the previously determined ring geometry.

Because this is an often-used procedure, implemented e.g. by the *reswri* tasks (which uses *ROTCUR* as the first step) within the *GIPSY*<sup>6</sup> package, we decided to test the applicability of this approach. We follow a two-step procedure. First, a tilted ring analysis of first order is performed, where we allow inclination and position angle to vary fully independently for each ring. In a second step, a Fourier decomposition of the velocity field is calculated, in which inclination and position angle are fixed to the values determined in the tilted ring fit. We compare two slightly different methods. In the first one, the initial tilted ring fit already includes radial motions in the form of the  $V_{\text{rad}}$  term in equation (4). In the second one, it is restricted to a purely rotational velocity field. The latter is similar to the one used by Schoenmakers et al. (1997) and Trachternach et al. (2008). Technically, they performed the Fourier decomposition not on the full velocity field, but instead on the residuals of the tilted ring fit. None the less, in this approach it means the ring geometry is derived from a purely rotational tilted ring fit.

The results of our comparison of the two schemes applied to the NGC 2403 data are presented in Fig. 2. The derived rotation curves turn out to be nearly identical and also the inclinations are very similar. The measured position angle is systematically higher in the

case where no radial motions are permitted in the tilted ring fit. The deviation in position angle of  $6^\circ$  appears small and may be dismissed as not significant at first glance; however, it causes the measured  $s_1$  component in the Fourier decomposition to change substantially. If the ring geometry is determined without taking radial motions into account, the subsequent Fourier analysis is not able to recover any significant radial velocities in the second step of the analysis. The  $s_1$  component varies between 0 and  $-2.5 \text{ km s}^{-1}$ , which can be taken as a null result. This is in general agreement with the results of Schoenmakers et al. (1997) and Trachternach et al. (2008), who also find little evidence for radial gas motions.

If in turn radial motions are already allowed in the tilted ring fit, the conclusions change and we find clear signs of radial inflow. The  $s_1$  component is always well below zero and shows a large feature between radii of 350 and 900 arcsec with a maximum inflow velocity of  $15 \text{ km s}^{-1}$ . In this scheme, the radial motions are already part of the tilted ring fit, which itself does not depend on any a priori assumptions except the centre position. We conclude that taking the radial velocity term into account in the first analysis step makes this approach more general and allows us to recover a radial velocity flow if it is present in the data.

To better quantify the differences between the two approaches, we create a synthetic velocity field, similar to the one derived from the NGC 2403 data. We choose the disc to be flat with a constant position angle of  $122^\circ$  and an inclination of  $60^\circ$ . For the rotation velocity, we adopt a rotation curve of Brandt-type (Brandt 1960) in the rising part and a constant velocity of  $135 \text{ km s}^{-1}$  outside of 500 arcsec. To this ideal disc, we add an inflow component starting at a radius of 350 arcsec and linearly increasing to  $15 \text{ km s}^{-1}$  at

<sup>6</sup> Groningen Image Processing System: <http://www.atnf.csiro.au/computing/software/gipsy/index.html>

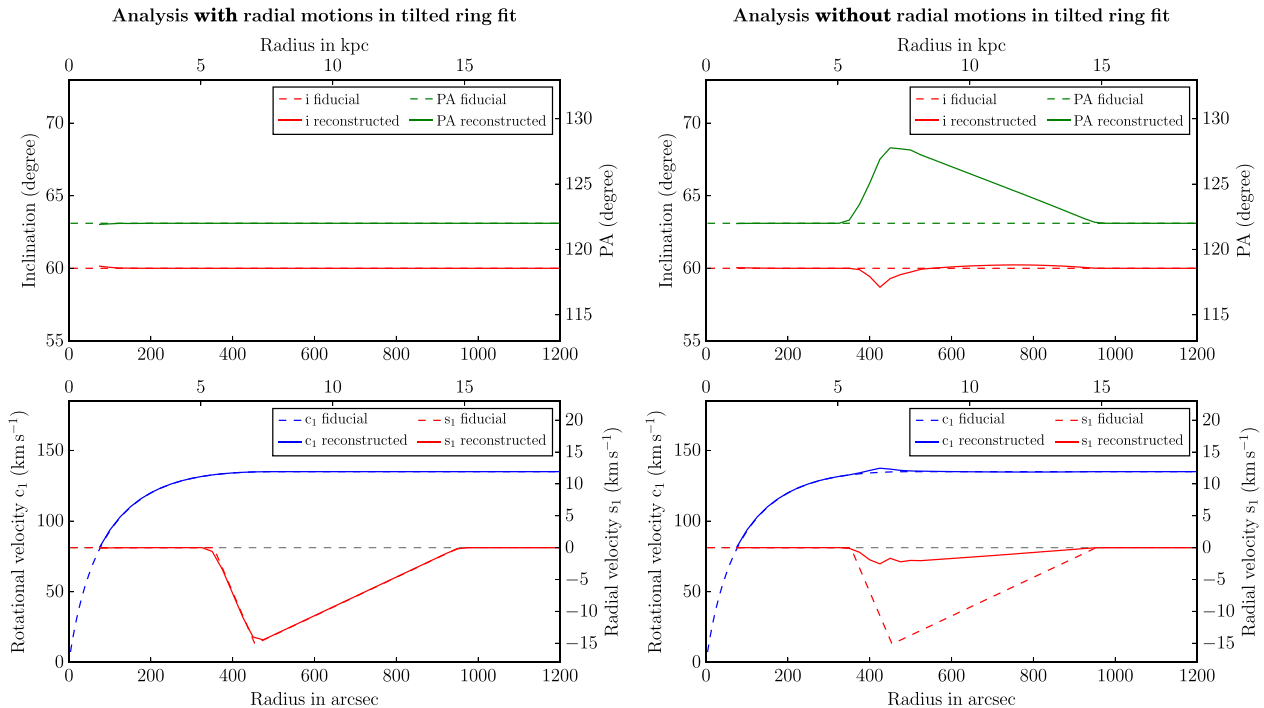


**Figure 3.** The two different two-step fitting procedures (with and without a radial velocity term in the tilted ring fit) applied to a synthetic velocity map that roughly resembles the one for NGC 2403. In each plot, the input values used to create the artificial data are shown as thin dashed lines. The plots on the left-hand side show the results derived by the fitting scheme which includes radial motions already in the tilted ring fit. The input values are exactly recovered, i.e. for  $i$ , PA and  $V_{\text{rot}}$  input values and fit results are indistinguishable. For the  $s_1$  component, the plot shows minor deviations. The results of the scheme in which the ring geometry is determined without taking radial motions into account are shown on the right-hand side. During the initial tilted ring fit, the position angle is fitted to a value that compensates for the radial motion (upper-right panel). In the subsequent Fourier decomposition, only a small fraction of the actual radial velocity signal is recovered. The Fourier decomposition is not able to find the correct inflow because it is restricted to the wrong ring geometry.

450 arcsec. It then declines again linearly and returns back to zero at 950 arcsec. The exact shape of the rotation curve is not crucial, since the inflow we try to recover happens only in the flat part of the rotation curve.

We then fit this velocity field in the same way we treated the NGC 2403 data. We first apply a scheme that includes a radial component already in the tilted ring analysis, and then use the method that does not take it into account. Noise is not added to the mock data since our focus is solely on the systematics of both methods. In addition, simple Gaussian noise would largely average out due to the huge number of data points in the mock velocity map. The results are shown in Fig. 3.

The analysis with inflow in the tilted ring stage perfectly recovers all parameters. There are only small deviations of the  $s_1$  component in the innermost parts of the disc and some finite-resolution effects. The solid curves representing the fit are indistinguishable from the dashed lines representing the input of the mock velocity field and most importantly, the fit recovers the correct inflow pattern.

In contrast to this, the analysis method that does not include radial motions in the tilted ring fit is not able to properly recover the radial flow. It shows some signal in the  $s_1$  component, but the maximum amplitude of  $\approx 3 \text{ km s}^{-1}$  is only a small fraction of the correct value. One can see that the position angle determined in the tilted ring analysis yields an incorrect value to compensate for the inflow. The deviation is roughly proportional to the radial velocity and peaks at a mismatch value of about  $6^\circ$ . The overall picture is similar to the deviation between the two methods seen for the NGC 2403 data. Since the radial velocity component is already compensated for by the disc geometry in the tilted ring stage, the subsequent

Fourier decomposition cannot recover more than a small residual  $s_1$  component, and thus disguises potential signatures of substantial radial gas motions.

### 3.4 Simultaneous fit

As demonstrated above, it is necessary to include the radial velocity component already in determining the ring geometry. The next question is, what happens to the second or higher orders in the Fourier decomposition. From our experience with fits to mock velocity fields, we come to the conclusion that the second-order terms do not couple to  $i$  and PA in a significant way. It should therefore be no problem to fit them in a subsequent step, once the ring geometry was determined in a tilted ring fit. However, since they are orthogonal not only to the first-order terms, but also to  $i$  and PA, there is also only a minor additional complication to fit them all simultaneously. To avoid any issues from carrying out a fit in two distinct steps, we investigate a fitting scheme where we fit inclination, position angle and all velocity components up to second order at the same time. Compared to the two-step approach including radial motions in the tilted ring analysis, the simultaneous fit yields nearly identical results. It is equally reliable and stable.

Before outlining the details of the simultaneous fitting approach that we apply to the THINGS data in Section 3.5, we comment on the prospects of including terms that are higher than second order in the Fourier decomposition. We find that this is a difficult exercise. For example, the  $c_3$  component is highly degenerate with the inclination. This makes a simultaneous fit of  $c_3$  and  $i$  impossible. One cannot compare the results of a two-step approach to a simultaneous fit of



third order. A third-order Fourier decomposition based on a disc geometry determined in a first- or second-order analysis cannot yield the correct value for the  $c_3$  term. The parameter  $c_3$  is implicitly assumed to be zero in the first step, and so the inclination is fitted to a value that compensates for a possible non-zero  $c_3$  term. One could in principle fix  $c_3$  and fit everything else up to fourth order, but there is no justification for assuming the  $c_3$  component to vanish or to be of any particular form while at the same time trying to measure the  $s_3$  and higher components. Therefore, it seems there is no satisfying way to safely deduce higher than second-order Fourier parameters without the risk of systematic errors, at least not from the velocity field alone and in a purely kinematic approach. It is for this reason that we restrict our analysis to a simultaneous fit of second order in  $V_{\text{los}}$ . This limits the level of detail we can derive but on the other hand reduces the necessary assumptions and related systematics to an absolute minimum while also making the model as flexible as possible since everything is fitted simultaneously.

### 3.5 Fit procedure

The model we finally adopt is a second-order Fourier decomposition of the following form:

$$V_{\text{los}} = V_{\text{sys}} + \sin(i)[c_0 + s_1 \sin(\theta) + c_1 \cos(\theta) + s_2 \sin(2\theta) + c_2 \cos(2\theta)]. \quad (9)$$

The coordinates of the disc frame  $(R, \theta)$  are related to the sky coordinates  $(X, Y)$  by equations (2) and (3). The coordinate transformation itself depends on the galaxy centre, the inclination and the position angle. We fit all five Fourier parameters  $(c_0, s_1, c_1, s_2, c_2)$  as well as  $i$  and PA for each ring simultaneously. The centre coordinates  $(X_C, Y_C)$  and the systemic velocity have to be determined in advance and are kept fixed for all rings. We do that by fitting a simple tilted ring model in which  $V_{\text{sys}}$  and the centre coordinates are free to vary to the innermost area of the velocity field. In this part of the disc, the fit is stable even without assuming a fixed centre. We then take the average values of the ring fits. The choice of  $V_{\text{sys}}$  only influences the  $c_0$  component in the Fourier decomposition. All other parameters are unaffected by that and an incorrectly chosen  $V_{\text{sys}}$  remains transparent throughout the analysis.

The ring widths are chosen for each galaxy individually to get the best compromise between good sampling and fit stability. Typical widths are between 24 and 48 arcsec which is always larger than the THINGS synthesized beam width of  $\approx 11$  arcsec (Walter et al. 2008). In the common case of warped discs, gaps naturally appear between rings and the observational data within the gaps of our tilted ring model are unused. To alleviate this effect to some degree and to make maximal use of all available data, we choose the separation of adjacent rings to be 37 per cent smaller than the width of the rings. This closes most of the gaps in the model but also leads to some overlap of rings. The exact amount of overlap depends on the fitted ring geometry. Since each ring is fitted individually and independently of all other rings, the overlap has no influence on the fit result. The only consequence is that neighbouring rings are statistically slightly correlated (however, omitting every second ring in our analysis and the following figures leads to a statistically independent sample).

We start the fit procedure with the central ring. After the fit for this ring has converged, the fit results are taken as initial values for the second ring. This procedure of outward forwarded initial values is used for all succeeding rings. We only have to manually set the initial values for the central ring to reasonable starting values. Their

exact choice has negligible impact on the overall result. In general, the question of whether the fit for a particular ring converges or not depends more strongly on the quality of the data and on possible irregularities in the velocity field than on the given initial conditions. For good quality data, the fit converges to the right value even if extremely poor guesses for the initial conditions are made. For disturbed discs, low inclinations, and especially velocity fields with linearly rising rotation curves, the rings have the tendency to flip to a very high inclination. This often happens in the innermost parts of the galaxies, and is likely caused by solid-body rotation and bars. If this affects only the few innermost rings, we can simply ignore them and use the well-fitted outer part, since this is where our scientific interest is focused on.

Linearly rising rotation curves make it impossible to disentangle  $i$  and  $V_{\text{rot}}$ . It can especially in the centre of galaxies happen that the fit converges to obviously incorrect values ( $i$  very close to 90). If this affects only a few rings in the galaxy centre while the other rings are fine, we discard the obviously wrong ones and keep the rest.

After the ring fit is completed, we calculate the  $V_{\text{rad}}$  and  $V_{\text{rot}}$  parameters according to equation (8). As mentioned before, the degeneracy between  $B_1$  and  $C_1$  cannot be broken and we assume  $C_1 = B_1$ .

The final step is to convert velocities to mass flow rates. From the derived Fourier parameters, we construct a two-dimensional synthetic radial velocity field by taking only Fourier components of radial direction into account. To convert the THINGS H I integrated line intensity (zeroth-moment) maps to column densities and finally to H I mass surface density, we adopt the method and distances given in Walter et al. (2008) and assume the H I gas to be optically thin. The THINGS first-moment maps represent an intensity-weighted and therefore approximately mass-weighted mean velocity at each position  $(R, \phi)$ . As outlined above, we decompose these velocities into a rotational,  $V_{\text{rot}}(R, \phi)$ , and radial,  $V_{\text{rad}}(R, \phi)$ , component. In order to compute a 2D distribution of the radial mass flow rate, we simply need to multiply  $V_{\text{rad}}(R, \phi) \times \Sigma_{\text{H I}}(R, \phi)$  for each position. To obtain the net flow rate at each radius, we integrate over the azimuthal angle  $\phi$ :

$$\Gamma_{\text{rad}}(R) = \int_0^{2\pi} V_{\text{rad}}(R, \phi) \Sigma_{\text{H I}}(R, \phi) R d\phi. \quad (10)$$

Here,  $\Gamma_{\text{rad}}(R)$  denotes the radial mass flow rate and  $\Sigma_{\text{H I}}$  the H I mass surface density. We note that radial velocities can be directed inwards or outwards so that  $\Gamma_{\text{rad}}(R)$  represents a net flow rate. We also note that in practice we calculate  $\Gamma_{\text{rad}}(R)$  in radial bins of finite width  $\Delta R = 24\text{--}48$  arcsec (compare description earlier in this section). We interpret these radial H I net mass flow rate profiles and compare them to SFR profiles of our galaxy sample in Section 3.7.

### 3.6 Error estimation

For the fit procedure described in Section 3.5, we use a standard  $\chi^2$ -optimizer, which also gives formal statistical uncertainties. However, in order to obtain more realistic uncertainty estimates, we carry out additional Monte Carlo modelling. That is, we add random noise with specific characteristics to our data and measure how this influences the results. We repeat this 100 times to build up a statistically significant sample.

We point out that adding purely Gaussian noise would not serve our purpose, because it would average out due to the large number of data points in the H I maps. We are more concerned about potential systematic patterns in the velocity field that we cannot account for in

our fitting routine. Sellwood & Sanchez (2010) advertise a concept that uses the residuals of the fit as a noise source. The idea is that every residual structure not included in the model is in fact noise to the fit, and the residuals can be used as a prior to create a noise field with statistical characteristics that are well matched to the data. The authors randomize and resample the two-dimensional map of the residual by rotating and shifting chunks of it in radius by random amounts. This creates a statistical noise field, but it also preserves any structures and coherence on small scales.

We follow the same approach, but we modify the resampling procedure since in our model inclination and position angle are allowed to vary throughout the disc. We therefore do not deal with one continuous velocity field but instead with an ensemble of tilted rings that can in general have gaps and overlapping regions. We therefore apply this procedure to each ring individually. The exact procedure we use is the following: after the fit, we calculate for each ring the residual after subtracting the fit from the data. Each residual is deprojected according to the ring geometry determined in the fit, and it is rotated around the ring centre by an individual angle, randomly chosen between  $-\pi$  and  $\pi$ . It is then reprojected using the same geometry. An artificial noise map is created by combining all rings, which is then added to the observed velocity field. The perturbed data cube is then fitted again. The resulting residuals are resampled in the same way and added to the original data to be used in the next iteration. We repeat this procedure 100 times, and so obtain an ensemble of 100 values for our fit parameters. From this, we compute mean and standard deviation which we take as our final results. We investigated the number of iterations necessary for convergence by running up to 2500 iterations and found that 100 is sufficient.

### 3.7 Comparing radial H I mass fluxes to SFRs

The processes that transport gas within a galaxy and transform it into stars are complex. In order to compare our H I radial flux measurements to the SFR profiles, we present a simplified model that is solely based on mass continuity arguments:

$$\frac{d}{dt} \int_A \Sigma_{\text{H I}} dA = - \oint_{\delta A} \mathbf{F}_{\text{H I}} d\mathbf{l}. \quad (11)$$

$\Sigma_{\text{H I}}$  is the H I column density or the equivalent H I mass surface density and  $\mathbf{F}_{\text{H I}}$  the H I mass flux density. We assume the disc to be thin and therefore only deal with a two-dimensional problem. If we include the star formation rate surface density  $\Sigma_{\text{SFR}}$  as a sink term on the left-hand side, focus only on the radial mass flux and use Gauss' theorem to express everything in local quantities, we find

$$\frac{d}{dt} \Sigma_{\text{H I}} - \Sigma_{\text{SFR}} = - \frac{d}{dr} F_{\text{rad}}. \quad (12)$$

For this study, we only deal with azimuthally averaged quantities. This justifies ignoring rotational streaming in the previous step and leads to the following relation:

$$\int_0^{2\pi} \left( \frac{d}{dt} \Sigma_{\text{H I}} - \Sigma_{\text{SFR}} \right) r d\phi = - \frac{d}{dr} \int_0^{2\pi} F_{\text{rad}} r d\phi. \quad (13)$$

The quantity  $\Gamma_{\text{rad}} = \int_0^{2\pi} F_{\text{rad}} r d\phi$  is our measured radial mass flux profile.

We note that we do not take into account the contribution from helium when we quote H I masses or surface densities (a factor of 1.36). For an appropriate description, one probably also has to add additional sink and source terms to the left-hand side. These could for example reflect stellar winds and outflows, galactic fountains or

gas that condenses from the hot halo gas or circumgalactic medium and settles to the disc. These processes are in general difficult to model and beyond the scope of this toy model. However, if we measure a violation of equation (13), we have an indication that some of these processes may be present.

If one assumes the special case that star formation and other sink and source terms vanish and observes the radial mass flux to be constant (but not necessarily zero) over some radial range, then the H I column density should not change with time and the galaxy would be in a (quasi) stationary state. On the other hand, if  $\frac{d}{dr} \Gamma_{\text{rad}}$  is negative, gas should pile up.

If we assume our galaxies to be in such a stationary state and therefore  $\frac{d}{dt} \Sigma_{\text{H I}} = 0$ , the mass flux at a given radius equals the total star formation within this radius:

$$\int_0^R \int_0^{2\pi} \Sigma_{\text{SFR}}(r, \phi) r d\phi dr = - \int_0^{2\pi} F_{\text{rad}}(R, \phi) r d\phi. \quad (14)$$

This is a relation we can test by comparing our radial mass flux measurement to cumulative SFR profiles, which we derive from *GALEX* FUV data. For this, we closely follow the procedure described in Bigiel et al. (2010a) and use the conversion factor from Salim et al. (2007). We take the ring geometry from our kinematic analysis and for each ring compute the total SFR from the galaxy centre out to this radius. We correct for Galactic extinction according to Schlafly & Finkbeiner (2011) and blank bright stars but neglect extinction within the target galaxies. A detailed comparison of the various SFR calibrations using different tracers (e.g. H $\alpha$ , UV or IR emission) is beyond the scope of this study. To be consistent with accurate, published galaxy integrated SFRs, we scale our cumulative SFR profiles to match the literature values (Table 1) at large radii, which is equivalent to assuming a constant intrinsic extinction. We note that this approximation is sufficient for the purposes of this study, and any more accurate treatment of internal extinction at small radii does not affect our conclusions.

As we show in Section 5, the naive assumption of vanishing time dependence and absence of other processes is rarely appropriate, but the deviations from this simplified model might give insights on the magnitude of other processes.

## 4 VERIFICATION OF THE METHOD

As we show in Section 3.3, the overall fitting scheme can be in general quite sensitive to prior assumptions. We therefore conduct a suite of tests in order to assess the correctness of our results and to determine the potential limitations of our approach. We focus mostly on the analysis of synthetic velocity fields and on testing under which conditions the input values can be recovered correctly. But we also investigate the dependence of our results on the type of velocity maps (such as intensity-weighted first-moment or Hermite) that are used.

### 4.1 Limits of the method

In Fig. 3, we demonstrate that a two-step fit with radial components at the tilted ring stage is perfectly able to recover radial motions from a synthetic velocity field, at least if the disc is flat. This is also true for the second-order simultaneous fit scheme introduced in Section 3.5 which is used for the rest of the paper. However, galactic discs are not flat, but instead they exhibit warps and changes of position angle. Both constitute a great challenge for any tilted ring like analysis, because the deprojection of the velocity field is no longer continuous and unique.

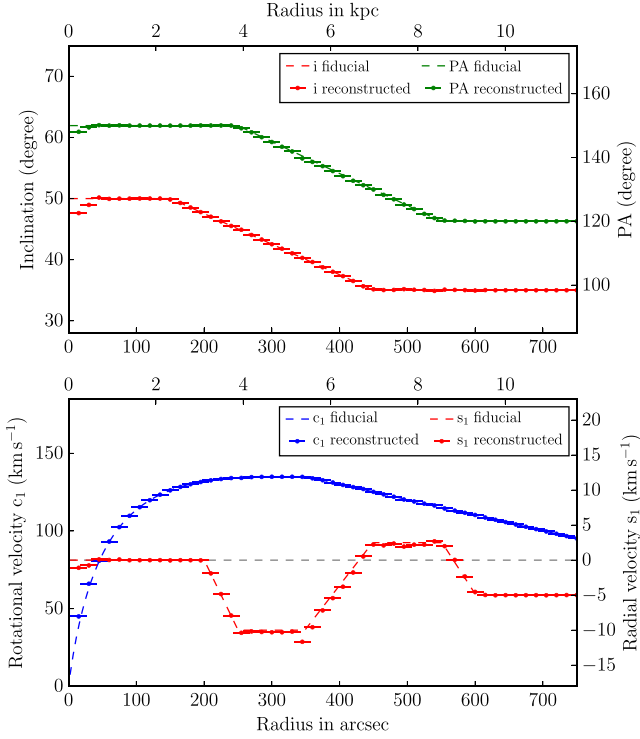


**Figure 4.** Our method applied to a synthetic velocity field. Even if geometry and velocity parameters of the mock data deviate in different patterns and at different, overlapping radial ranges from a flat disc, the analysis is able to recover all of these features with high precision.

In Fig. 4, we show an example of a fit to a synthetic velocity field with mild warps and position angle changes. We start again with a flat disc with a Brandt-type rotation curve. It is then modified by a decrease in inclination  $i$  by  $15^\circ$  over 300 arcsec in radius, a change of position angle PA by  $30^\circ$  over 300 arcsec and a decrease of rotation velocity of  $10 \text{ km s}^{-1}$  per 100 arcsec starting at 350 arcsec. In addition, a pattern of in- and outflows of different magnitude up to  $10 \text{ km s}^{-1}$  is added. All these single effects cover different radial ranges. Therefore, a variety of combinations of effects are simulated at the same time. Again, since we are interested in systematic effects, no noise is added to the artificial velocity field.

The plots in Fig. 4 show that our method can fully recover the parameters of the input velocity field to a very high accuracy. Problems only occur, as expected, at very small radii. In addition, a slight tendency for deviations exists at points where the slope of parameters abruptly changes. But overall, the result is highly satisfactory. So, our method is valid at least for mildly disturbed discs.

In the following, we will address how our fitting procedure reacts to stronger warps. Generally, a decrease of inclination with radius will not be a problem, but a strong increase will be.

Taking two annuli with radii  $R_1, R_2, R_1 < R_2$  and inclination angles  $i_1, i_2, i_1 < i_2$ , their apparent semiminor axes have the projected length  $R \times \cos(i)$ . If  $R_1 \times \cos(i_1) = R_2 \times \cos(i_2)$ , the two annuli completely overlap on the minor axis and our assumption of a thin disc with unique line-of-sight velocities is no longer valid. This condition can be converted to an expression for the maximum inclination increase that does not lead to a pile-up of rings on the minor axis:

$$\left(\frac{\Delta i}{\Delta R}\right)_{\text{crit}} = \frac{1}{R \tan i}. \quad (15)$$

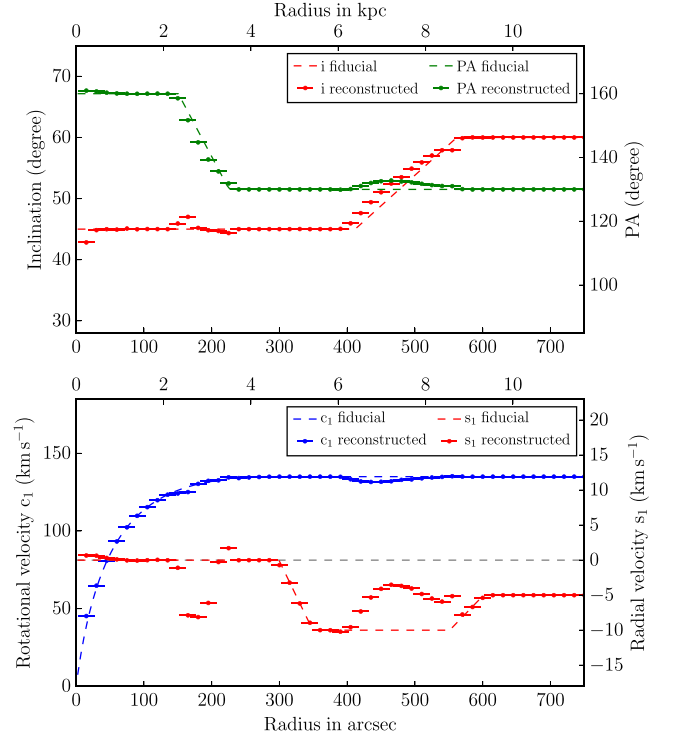


**Figure 5.** Fit to a velocity field that shows much stronger changes in position angle and inclination than the one used in Fig. 4. Obviously, the analysis is not anymore capable of fitting these data correctly. The steep increase of  $i$  with nearly twice the critical rate derived in equation (15) causes a mismatch of all parameters. The errors in  $i$ , PA and  $V_{\text{rot}}$  seem small but they result in a significant error in the  $s_1$  term of up to  $7 \text{ km s}^{-1}$ . Also, the change in PA at  $R \approx 200$  arcsec is now too fast to still allow a correct derivation of the  $s_1$  term.

Here,  $\Delta R$  denotes the increase in radius from one ring to the next and  $\Delta i$  the increase in inclination between the two rings,  $i$  and  $R$  are inclination and radius of the inner of the two rings.

While limited overlap of adjacent rings is in practice uncritical (and even enforced by the rings chosen 60 per cent wider), an inclination increase exceeding the critical rate will make even non-adjacent rings overlap. The apparent minor axis of the rings shrinks with increasing radius. In such conditions, the tilted ring approach breaks down.

Similar overlapping effect can also appear for changes of the position angle. Since the geometry of position angle changes is more complex, we do not derive an analytic expression for this case. In the end, it would anyway be necessary to consider the combined effect of inclination and position angle changes, which complicates things even further.

Our experiences with fits to synthetic velocity fields are in good agreement with the above analytic considerations. In the cases where the inclination decreases (e.g. Fig. 4) or increases with less than the critical rate given in equation (15), we see no significant deviations. If the inclination is increased close to the critical rate, some noticeable deviations appear, but the derived results are still usable with less than  $1.5 \text{ km s}^{-1}$  maximum error for the  $s_1$  component (not shown). However, much larger changes of the inclination angle cause strong artefacts in the fit results. This is illustrated in Fig. 5, where the inclination angle changes with twice the critical rate. At the warp, the inclination is typically fitted to a too high value. This is because data at larger radii interfere with those from smaller radii. In addition, also the position angle and the rotation

velocity are fitted to a slight mismatch. At first glance, these deviations do not appear severe; however, as discussed earlier, they lead to large deviations for the important  $s_1$  parameter, with errors of  $5 \text{ km s}^{-1}$  and more over a large range in radius. This is of the same order of magnitude as potential inflow velocities, and therefore can render the fit result useless. Interestingly, no deviation for the radial component is seen if the  $s_1$  component in the synthetic velocity field is set to zero, although the derived values for  $i$  and  $c_1$  actually differ from the input.

Also visible in Fig. 5 is an artefact in the  $s_1$  curve due to a rapid change of the position angle, which is not perfectly accounted for. The inclination and rotation curve stay quite stable with only minor deviations, but the radial velocity shows incorrect peaks of up to  $10 \text{ km s}^{-1}$ . The  $30^\circ$  change in PA over only 75 arcsec in radius is a very fast one. If this change is stretched over 150 arcsec, we find only small deviations of less than  $1 \text{ km s}^{-1}$ . At a rate of  $30^\circ$  over 300 arcsec as in Fig. 4, any significant deviations have vanished.

We also investigate the influence of an incorrect determination of the galaxy centre. Our tests showed that an offset of the order of a few arcseconds away from the true centre is not critical for our analysis. It creates artefacts, but their amplitude quickly decreases towards larger radii. For example, offsets of the order of 5 and 10 arcsec are no longer noticeable outside of 100 and 200 arcsec, respectively. We conclude that the uncertainties involved in determining the galaxy centre are therefore not an issue within the context of this study.

#### 4.2 Comparison of first-moment and Hermite velocity maps

First-moment maps are often employed to derive velocity maps from data cubes. They are easy to compute and do not require very high S/N levels. However, if the line profile is asymmetric or has extended wings, this method does not properly represent the bulk velocity of the gas. We therefore also include velocity maps from de Blok et al. (2008) in our analysis. These are based on fitting Gauss–Hermite functions to the H I spectra of each spatial resolution element. By modifying the Gauss function by the third-order Hermite polynomial, the fitting function is capable of adapting to asymmetric line shapes and in this case better represents the bulk velocity. A detailed description can be found in van der Marel & Franx (1993).

We apply our method to the galaxy NGC 2403 and compare the standard moment map provided by THINGS to the corresponding Hermite map. The result is illustrated in Fig. 6. Both velocity maps do not give exactly the same result but they are in general agreement. The most obvious difference lies in the intermediate part of the galaxy. In the moment map, we find a maximum inflow velocity of  $15 \text{ km s}^{-1}$  at 450 arcsec. The inflow then linearly decreases to  $3 \text{ km s}^{-1}$  at 900 arcsec. The Hermite map shows even more inflow at around 500 arcsec followed by a rapid decrease to a roughly constant inflow velocity of  $6 \text{ km s}^{-1}$  between 600 and 800 arcsec. Besides this, the results are quite similar and most importantly, both maps show the same unambiguous signs of large-scale inflow.

Unfortunately, fitting Hermite functions to the data cube requires substantially higher S/N compared to the moment maps. It can therefore not be applied to the outermost parts of the H I disc. Based on the results of this comparison, we decide to proceed using the moment maps for our analysis. The derived values for Hermite and moment maps approximately agree with each other and the moment maps extend further out from the galaxy centres which is particularly important for our aim of detecting large-scale radial inflow.

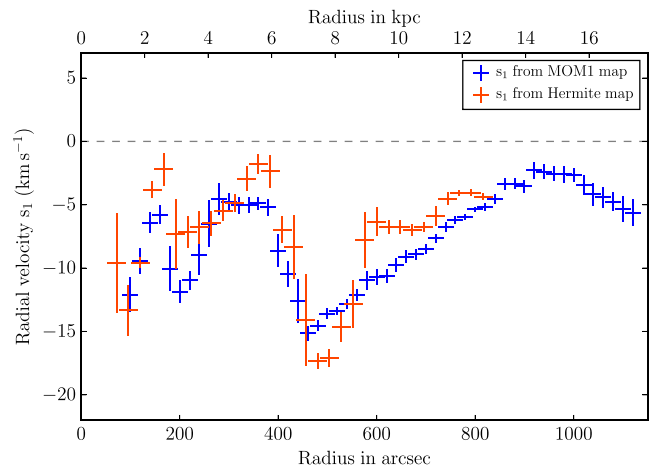


**Figure 6.** A comparison of the radial inflow pattern derived from a standard THINGS first-moment map and from a velocity map computed by fitting Hermite functions to the H I spectra. The Hermite map gives slightly different results than the moment map. From 450 to 550 arcsec, the inflow rate is higher, from 600 to 800 arcsec lower. However, the overall distribution of radial velocities is quite comparable. We note that the moment map extends to further radii, which is important for the analysis presented here.

## 5 RESULTS AND DISCUSSION

In the following section, we present our results. For each galaxy, we present four plots describing the fit parameters as functions of radius. Radius and velocities are measured within the galactic plane. For the exact details of the analysis, see Section 3.5. The four plots contain the following information:

- (i) inclination and position angle,
- (ii) the Fourier parameters  $c_1$  and  $s_1$ , which directly correspond to the principal components of the rotation and radial velocity, respectively,
- (iii) the Fourier parameters  $c_0$ ,  $c_2$  and  $s_2$ , which give information about the azimuthal dependence of the velocity field,
- (iv) the calculated radial H I mass flux, not accounting for helium, H<sub>2</sub> or other gas fractions and the cumulative SFR profile giving the total SFR within a certain radius based on *GALEX* FUV images and scaled to the more precise literature values given in Table 1.

The rotation direction of the galaxies is determined from optical images, especially from the more pronounced appearance of dark filaments on the nearside of the disc. By combining this information with the velocity field, one can distinguish if the galaxy is rotating clockwise or anticlockwise, which also determines if potential radial motion is directed inwards or outwards.

### 5.1 NGC 2403

In our sample of 10 THINGS galaxies, NGC 2403 turns out to be the most suitable target for detecting radial mass inflow patterns. It has a large apparent size of roughly  $16 \text{ arcmin} \times 10 \text{ arcmin}$ , was observed with good S/N ratio, and most importantly, it has a very flat and smooth H I disc and regular velocity field. Our fitting results are summarized in Fig. 8.

Position angle PA and inclination  $i$  are plotted as a function of radius in the top-left part of the figure. The galaxy is rotating clockwise, and so the south-western part of the disc is closer to Earth. The rotational velocity (Fourier component  $c_1$ ) is between 120 and



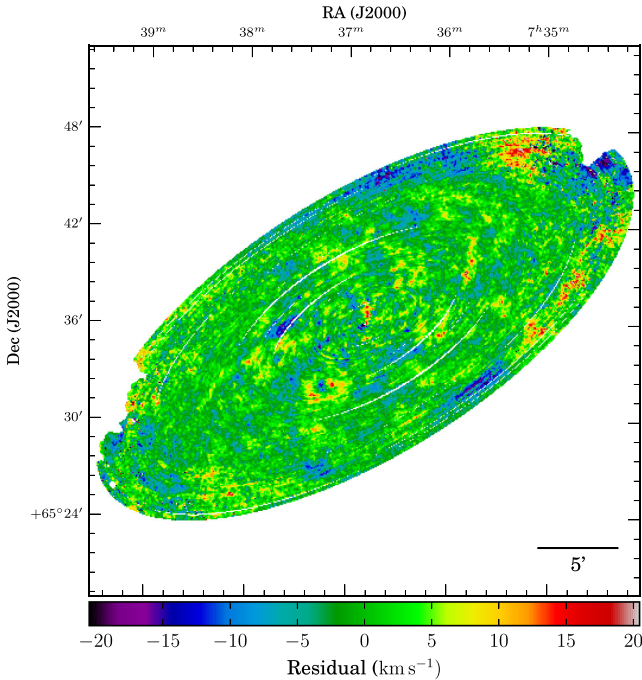


**Figure 7.** Residuals of the fit for NGC 2403. No distinct pattern of large-scale structure appears. A slight signature of spiral arms might be visible in the inner part.

$140 \text{ km s}^{-1}$ . As already described in Section 3.3, we find clear evidence for radial inflows. The derived radial velocity (Fourier component  $s_1$ ) is always negative with values of at least a few  $\text{km s}^{-1}$ . The most significant radial motion is found at radii between 400 and 900 arcsec (top-right panel of Fig. 8), and the strongest  $\text{H I}$  mass flux of  $3 \text{ M}_\odot \text{ yr}^{-1}$  is observed at 450 arcsec (Fig. 8, bottom-left panel). This mass flux linearly declines towards larger radii.

The quality of the fit we obtain for this galaxy is excellent. All parameters vary smoothly and adjacent rings show only very limited scatter. The residual deviations between data and our model (shown in Fig. 7) are of the order of  $\pm 10 \text{ km s}^{-1}$  and show no distinct pattern which would indicate a mismatch between fit and data. The flocculent spiral arms of NGC 2403 are just barely visible in the residual map. The terms  $c_0$ ,  $c_2$  and  $s_2$ , which indicate the deviation from a rotational symmetric velocity field, are fairly small inwards of 900 arcsec (Fig. 8, bottom-right panel). In the outskirts of the galaxy, there may be some lopsidedness. One can see some correlations between the different parameters around 200 arcsec. We cannot completely exclude that at this small radius a possible mismatch in e.g. the inclination induces artefacts in all parameters but these effects only appear in the inner part of the galaxy.

The SFR given in Leroy et al. (2008) is  $0.38 \text{ M}_\odot \text{ yr}^{-1}$ . This is of the same order as our minimum  $\text{H I}$  inflow rate but nearly an order of magnitude lower than our maximum inflow rate of  $3.5 \text{ M}_\odot \text{ yr}^{-1}$ . If we follow our highly simplified model described in Section 3.7, we would expect the radial mass inflow rate at all radii to equal the SFR within that radius according to equation (14). The bottom-left panel of Fig. 8 shows these two quantities and it is obvious that at most radii both quantities do not add up to zero. Also, we would expect the inflow to be monotonic with radius and to be highest at the outer edge of the  $\text{H I}$  disc. This is clearly not the case. Not surprisingly, there are probably additional processes other than inflow and star formation influencing the  $\text{H I}$  budget of NGC 2403.

One possible effect could be the ejection of ionized material from stellar winds perpendicular to the plane followed by recondensation and settling of that gas on to the plane at larger radii. This is often described as the galactic fountain model and could explain the additional mass flows. For NGC 2403 some indication for this was discovered by Fraternali et al. (2002). By taking position-velocity cuts parallel to the major and minor axis, they find substantial amounts of extraplanar  $\text{H I}$  gas that rotates more slowly than the disc and is reported to show a net inward motion. The gas they detect lies roughly in the same radial range (200700 arcsec) as the main inflow found in our analysis. However, our method has only limited sensitivity to extraplanar gas because its presence will not substantially change the intensity-weighted mean used to compute the moment maps. Another possible way to deviate from our stationary model is time-variable accretion, for instance if accretion happens via discrete events (e.g. large gas clouds).

The spatial correlation of inflow pattern and star formation is visualized in Fig. 9. It shows a composite of the *GALEX* FUV image and the reconstructed radial velocity field. The inflow has a maximum at 460 arcsec and decreases strongly at smaller radii. As described in Section 3.7, this should lead to a pile-up of gas or enhanced star formation. The *GALEX* image shows clear clustering of star formation regions in this area. Most of the star formation takes place inside of 200 arcsec, again a region where the magnitude of the inflow decreases. This spatial correlation may provide support, at least qualitatively, for a scenario in which  $\text{H I}$  inflows are a key parameter regulating star formation in this galaxy. However, a quantitative comparison shows that the amplitudes of SFR and inflow do not match, which may not be surprising since a variety of other factors (time evolution, stellar winds, gas phase changes, etc.) likely play an important role as well.

Our observation for NGC 2403 clearly shows a qualitative correlation between star formation and radial  $\text{H I}$  flows. This gives support to the picture that star formation may be regulated by inflows in NGC 2403. Meidt et al. (2013) analyse gravity-induced torques in the spiral galaxy M51, how they drive radial gas motions and how these are related to the local star formation efficiency. They find that radial motions seem to counteract star formation in this galaxy so that regions that experience higher torques show increased gas depletion times. This is the opposite sense of our finding here. M51 and NGC 2403, however, have quite different properties and are not immediately comparable. The spiral arms in NGC 2403 are by far not as pronounced as in M51 and the gravitational torques and dynamically driven inflows they might induce should be much lower and probably negligible. Our residual map (Fig. 7) indeed shows no signs of spiral arm structure. It is therefore not necessarily expected that the ‘dynamic pressure’ Meidt et al. (2013) describe suppresses star formation in NGC 2403 as it does in M51. Unfortunately, due to its low inclination, we cannot analyse M51 with the method presented in this study and directly compare the results.

## 5.2 NGC 2841

NGC 2841 has a very extended  $\text{H I}$  envelope, several times larger than the stellar disc and rotates anticlockwise which means the north-eastern part of the disc is the near side. Our fits to this galaxy are very stable and show a flat disc with very smoothly rising inclination and position angle (Fig. 10). The radial velocity (Fourier component  $s_1$ ) is close to zero up to a radius of roughly 550 arcsec. We find a small inflow in the range from 350 to 550 arcsec which is consistent with the reported SFR of  $0.74 \text{ M}_\odot \text{ yr}^{-1}$  (Leroy et al. 2008).

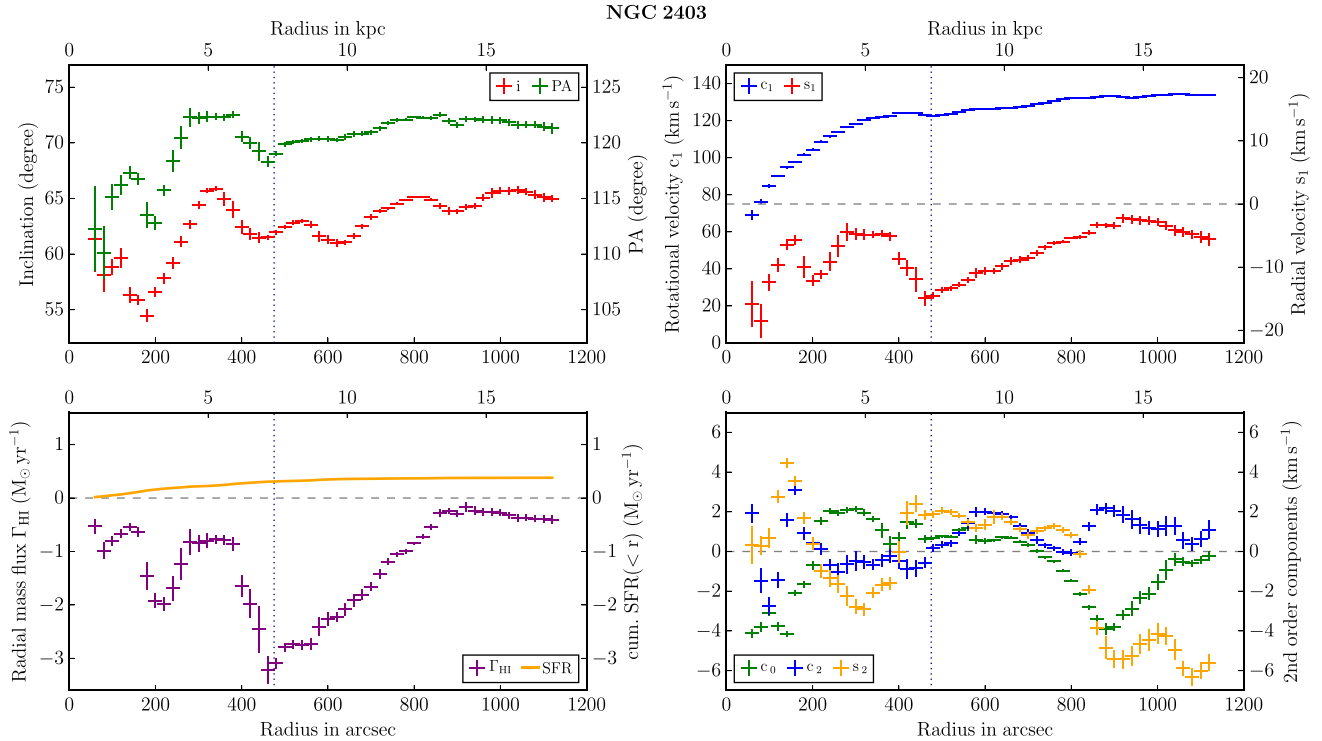


**Figure 8.** Disc geometry and Fourier parameters for NGC 2403. Horizontal error bars denote the ring width, and vertical bars represent the errors estimated according to the scheme described in Section 3.6. The dotted vertical line indicates the optical radius  $r_{25}$ . The galaxy shows a smooth and unperturbed disc. Position angle and inclination only vary within limited ranges (top-left panel). The radial velocity shows a very distinct signature between 400 and 900 arcsec (top-right panel, red points) with a peak inflow velocity of  $15 \text{ km s}^{-1}$  which corresponds to an H I mass flow of up to  $3 \text{ M}_{\odot} \text{ yr}^{-1}$  (bottom-left panel). The inflow quickly ceases inside of 400 arcsec and shows a second smaller feature at 200 arcsec. For very large radii, we find inflows of about  $0.5 \text{ M}_{\odot} \text{ yr}^{-1}$ . The bottom-left panel also gives the cumulative SFR. For NGC 2403, basically all star formation takes place within the central 7 kpc. The bottom-right panel displays the zeroth- and second-order terms which indicate the deviation from rotational symmetry.

From our SFR profile, we find that most of the star formation is located within 200 arcsec while we detect inflow between 300 and 600 arcsec.

Outside of 550 arcsec the radial velocity rises to  $25 \text{ km s}^{-1}$  which corresponds to an H I outflow of  $2 \text{ M}_{\odot} \text{ yr}^{-1}$ . The  $s_2$  term indicates some lopsidedness of this radial flow.

From the appearance of very pronounced dust lanes in visual images, it is clear that the galaxy rotates anticlockwise and the measured radial flow is indeed directed outwards. From the morphological appearance, one could speculate about tidal or merger effects; however, NGC 2841 is not accompanied by any major galaxy and only surrounded by several dwarf galaxies (an NED<sup>7</sup> search yields only minor companions with  $m_r > 15 \text{ mag}$  within  $3^\circ$  and  $\pm 400 \text{ km s}^{-1}$ ).

It is interesting to compare the H I distribution with the radial velocity field. A two-dimensional representation of this is given in Fig. 11. It shows the radial velocity field we reconstruct from the determined Fourier parameters as described in Section 3.5. Overplotted are contours of the THINGS integrated intensity map.

The H I distribution shows a prominent ring at intermediate radii. If a radial mass flow causes some accumulation of gas, we would expect this to happen as described in Section 3.7 at the location where the slope of  $\Gamma_{\text{rad}}$  is the most negative. From Fig. 10, we see that this is the case at around 360 arcsec. This radius is marked in Fig. 11 with a purple ellipse which exactly coincides with the

H I ring. A second, but weaker feature like this can be seen at 510 arcsec. This might indicate that our highly simplified model described in Section 3.7 even without any additional sink or source terms might actually provide a reasonable description for the mass flow processes in NGC 2841. Quantitatively, however, a mass flux with an amplitude of  $\approx 1 \text{ M}_{\odot} \text{ yr}^{-1}$  would have to act for a long time period to cause an enhancement in the H I distribution of NGC 2841, which has a total H I mass of  $8.6 \times 10^9 \text{ M}_{\odot}$ .

### 5.3 NGC 2903

NGC 2903 is rotating anticlockwise and has complex kinematics. Visual images and the HERACLES CO maps (Leroy et al. 2009) show a very clear bar structure which does not appear in the integrated H I maps. The bar in conjunction with the solid-body rotation in the inner regions prevents us from deducing proper fit results for radii smaller than 100 arcsec and also causes a quite complicated structure outside of this radius (see Fig. 12).

At 200 arcsec, our analysis shows a sharp minimum of the inclination, followed by a steep increase from  $55^\circ$  to  $67^\circ$  within 200 arcsec. This is close to the fastest inclination change rate we expect from equation (15) to still yield reliable fit results. We take this as an indication that the fit in this region is likely to be not very reliable. This dip in inclination furthermore coincides with two regions of very low H I flux, basically holes in the H I disc. In general, due to the complex kinematic structure of this galaxy, the fit results for radii below 250 arcsec could be affected by artefacts and should probably not taken at face value.

<sup>7</sup> <http://ned.ipac.caltech.edu>

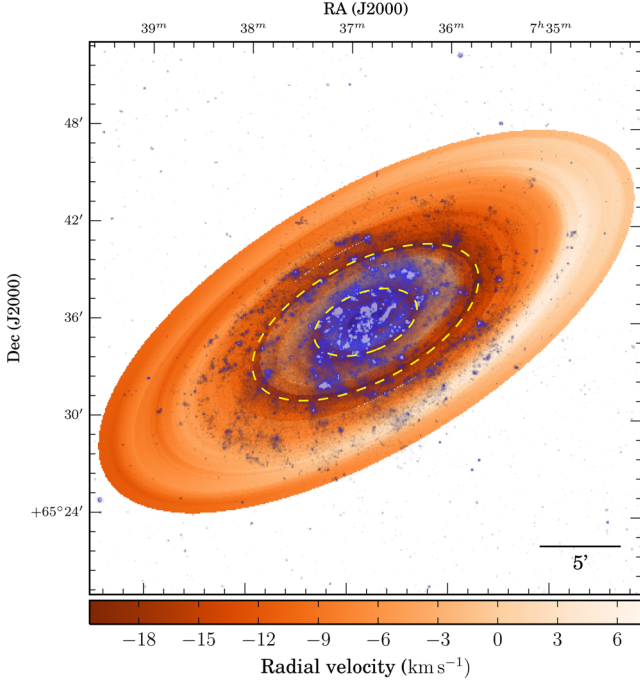


**Figure 9.** Combination of a reconstructed radial velocity field of NGC 2403 (orange shaded ellipses) and a *GALEX* FUV map tracing recent star formation. The yellow dashed ellipses mark radii of 200 and 460 arcsec, where the maximum inflow velocities are measured (compare to Fig. 8). It can be seen that most of the UV emission appears in the inner part of the disc, inside the region of peak inflow. This at least allows the interpretation that the gas moves inwards where it is transformed into stars.

The largest feature in our  $s_1$  curve is a massive inflow signature around 300 arcsec. Similar to NGC 2841, we can assess whether the radial gas motions could lead to the accumulation of gas in the ring structure visible in the integrated intensity map. Based on equation (13), we would expect a pile-up of gas at a radius between 200 and 300 arcsec due to the very steep negative slope of  $\Gamma_{\text{rad}}(R)$  but this region shows a rather low H I surface density. The ring structure is located at a radius of  $330 \pm 20$  arcsec. This does not correspond to any particular feature in the radial flux profile. The peak inflow at 300 arcsec also does not coincide, but is just inside the ring structure. In contrast to NGC 2841, our simple model described in Section 3.7 is obviously not able to describe the relation between radial motions and H I density in NGC 2903. We speculate that the ring structure might instead be related to more complex internal streaming motions, probably associated with the galactic bar, the effects of which are likely not captured correctly by our second-order analysis (de Blok et al. 2008). No further galaxy in our sample shows gas density features in sufficient detail to allow a straightforward comparison of radial motions to H I density. The absence of gas accumulation can always be explained by the low amplitude of the order of  $1 \text{ M}_{\odot} \text{ yr}^{-1}$  of the radial motions.

Further out beyond 500 arcsec, the kinematic structure of the disc seems less complicated and the velocity measurements indicate a quite substantial inward motion. However, due to the low gas surface densities at these radii, the corresponding H I mass flow rate is only  $0.3 \text{ M}_{\odot} \text{ yr}^{-1}$ . This is quite small but similar to the SFR reported by Popping et al. (2010), who report values ranging from  $0.4 \text{ M}_{\odot} \text{ yr}^{-1}$  derived from UV measurements up to  $1 \text{ M}_{\odot} \text{ yr}^{-1}$  from H $\alpha$  observations. Our own SFR measurement is consistent with Popping et al. (2010) but also shows that most of the star formation happens inside of 150 arcsec. Since our kinematic analysis does not yield reliable results in this region, a direct comparison is not

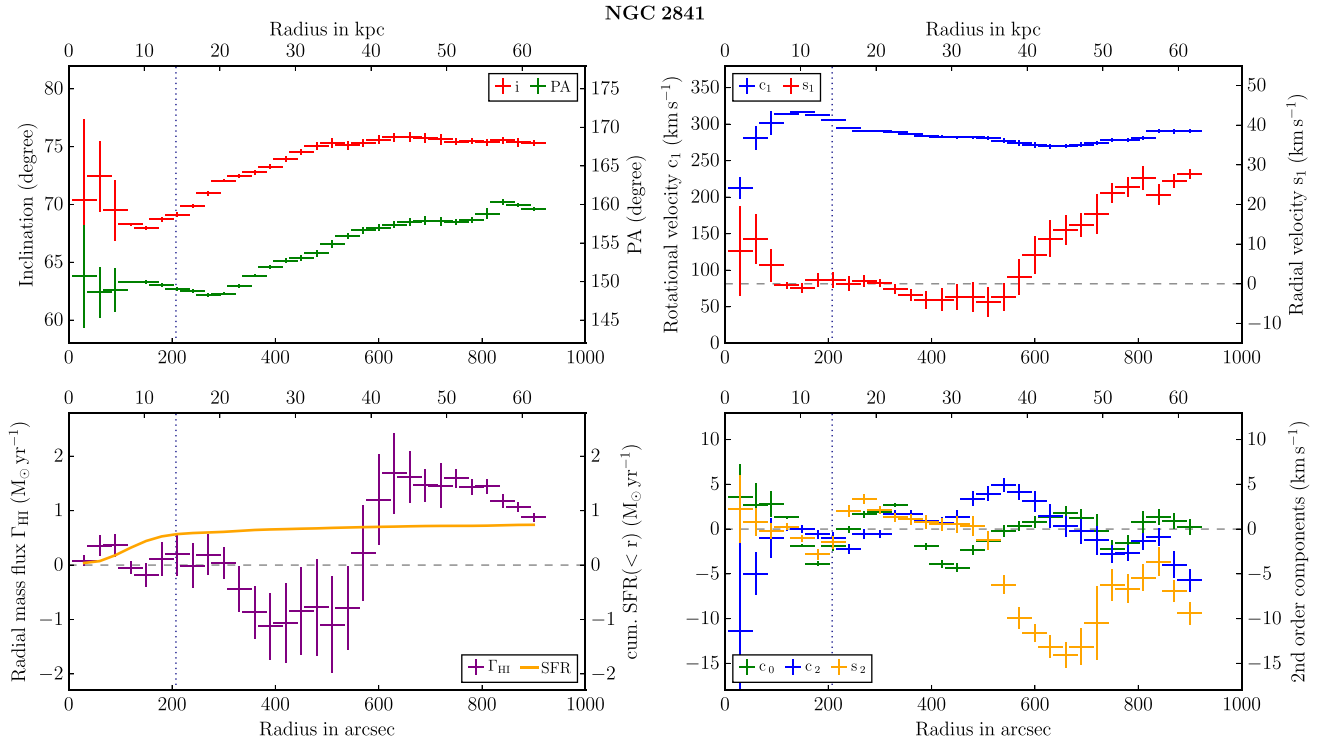


**Figure 10.** Disc geometry and Fourier parameters for NGC 2841. See the caption of Fig. 8 for technical details. The galaxy shows a fairly flat disc with a slight and smooth inclination increase in the inner half of the disc. Significant radial flows are only detected in the outer part, where gas seems to move away from the centre (red points in top-right panel).

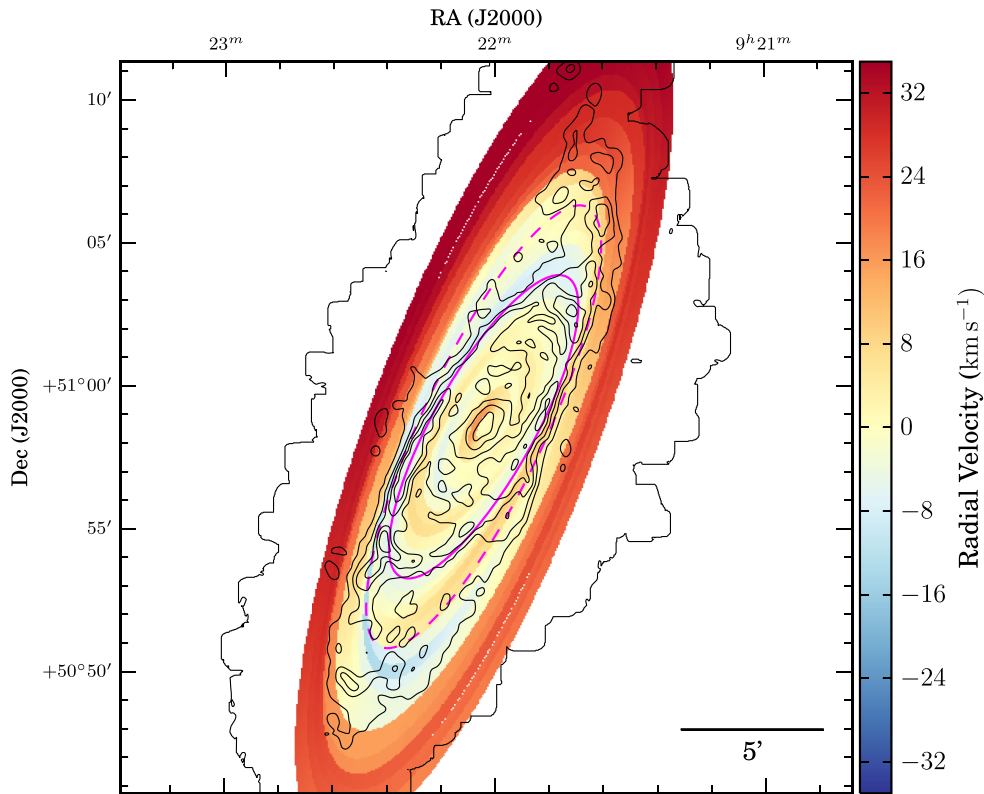


**Figure 11.** Two-dimensional representation of our derived radial velocity field of NGC 2841. The solid purple ellipse marks a radius of 360 arcsec at which the radial velocity has the strongest negative slope (compare to Fig. 10). At this radius, we expect according to equation (13) an accumulation of gas. The contours represent the H I density distribution which indeed shows a pronounced ring structure with enhanced gas density exactly at this radius. The dashed ellipse corresponds to 510 arcsec where we also find a fairly weak but in the southern half of the galaxy well visible negative slope in the radial velocity. This is as well spatially coincident with regions of increased H I density. It is therefore quite possible that radial gas motions and enhanced H I surface density are physically related.

possible. However, the data are still compatible with a scenario in which star formation inside of 150 arcsec is fuelled by the inflow visible in the disc beyond 500 arcsec.

#### 5.4 NGC 3198

NGC 3198 also rotates anticlockwise and the south-east part is the nearside. The galaxy has a flat disc without any substantial changes in inclination or position angle outside of 150 arcsec (Fig. 13).

The radial velocity we measure is always negative outside of 200 arcsec and we find significant inflow between 0.7 and  $2 \text{ M}_{\odot} \text{ yr}^{-1}$ . The average inflow outside  $r_{25}$  is  $1.1 \text{ M}_{\odot} \text{ yr}^{-1}$ . This agrees quite well with the SFR of  $0.93 \text{ M}_{\odot} \text{ yr}^{-1}$  reported by Leroy et al. (2008). Also the radial distribution is roughly consistent. Most of the star formation happens between 5 and 15 kpc. In this region, we find a substantial modulation of the inflow, probably caused by the star formation process, but outside of this radius we have a roughly constant inflow with an amplitude similar to the SFR. Therefore, the overall trend fits quite well in the picture that star formation is fuelled by inflows for this galaxy.

If we compare our results for the  $s_1$  component to the values obtained by Schoenmakers et al. (1997) and Trachternach et al. (2008), we find them to be very similar. We can reproduce their results by running a two-step analysis. Even if no radial flow is taken into account in the tilted ring fit, the subsequent Fourier decomposition shows clear signs of radial inflow with at least 50 per cent of the amplitude found in the simultaneous fit. This is somehow sur-

prising since for NGC 2403 neither Schoenmakers et al. (1997) or Trachternach et al. (2008) or our two-step fit could recover substantial radial inflows. For a detailed discussion of different fitting schemes and validations on mock velocity fields, see Section 3.3. Clearly, some property in the NGC 3198 velocity field is different compared to NGC 2403. As we show in Fig. 13, the  $s_1$  term is relatively small and the terms  $c_0$ ,  $c_2$  and  $s_2$  have comparable amplitude. This means, the asymmetry of the velocity field is of comparable amplitude as the overall net inflow. It may be possible that the inflow in this galaxy occurs in such a way that the tilted ring fit cannot adjust  $i$  and PA to fully compensate for the inflow. Indeed, inspection of the H I intensity map (available from the THINGS web page) shows an overall asymmetry with an extended north-east arm.

#### 5.5 NGC 3521

NGC 3521 is rotating anticlockwise and its western part is closer to us. Inclination, position angle and rotation velocity are fairly constant. The radial velocity seems to be of low amplitude, as depicted in Fig. 14. The SFR reported by Leroy et al. (2008) is  $2.1 \text{ M}_{\odot} \text{ yr}^{-1}$ . No GALEX FUV image was available in the data archive to derive an SFR profile (for the sake of consistency and comparability, we refrain from constructing this profile based on other SFR tracers).

We find a rather unusual behaviour for the  $c_0$  term, which starts to drop at about 200 arcsec and levels off at a value of  $-30 \text{ km s}^{-1}$ . The



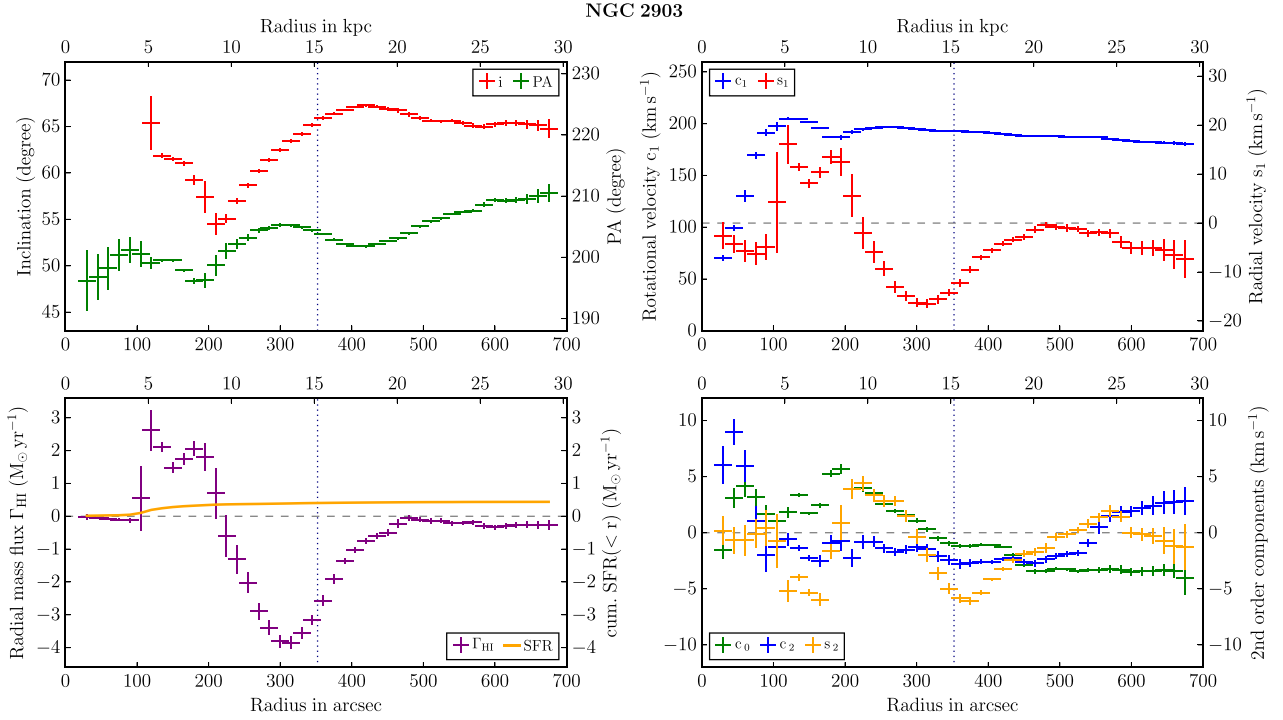


**Figure 12.** Disc geometry and Fourier parameters of NGC 2903. The galaxy shows a strong bar in visual images which seems to complicate the determination of the disc geometry in the innermost part. It is also not clear if the dip in inclination around 200 arcsec is a genuine feature or an artefact of the analysis (see the discussion in Section 5.3). The feature around 300 arcsec seems to be related to internal streaming motions. In the outskirts, the measured H I mass inflow is only around  $0.3 \text{ M}_{\odot} \text{ yr}^{-1}$ . However, this is still significant regarding the error estimates.

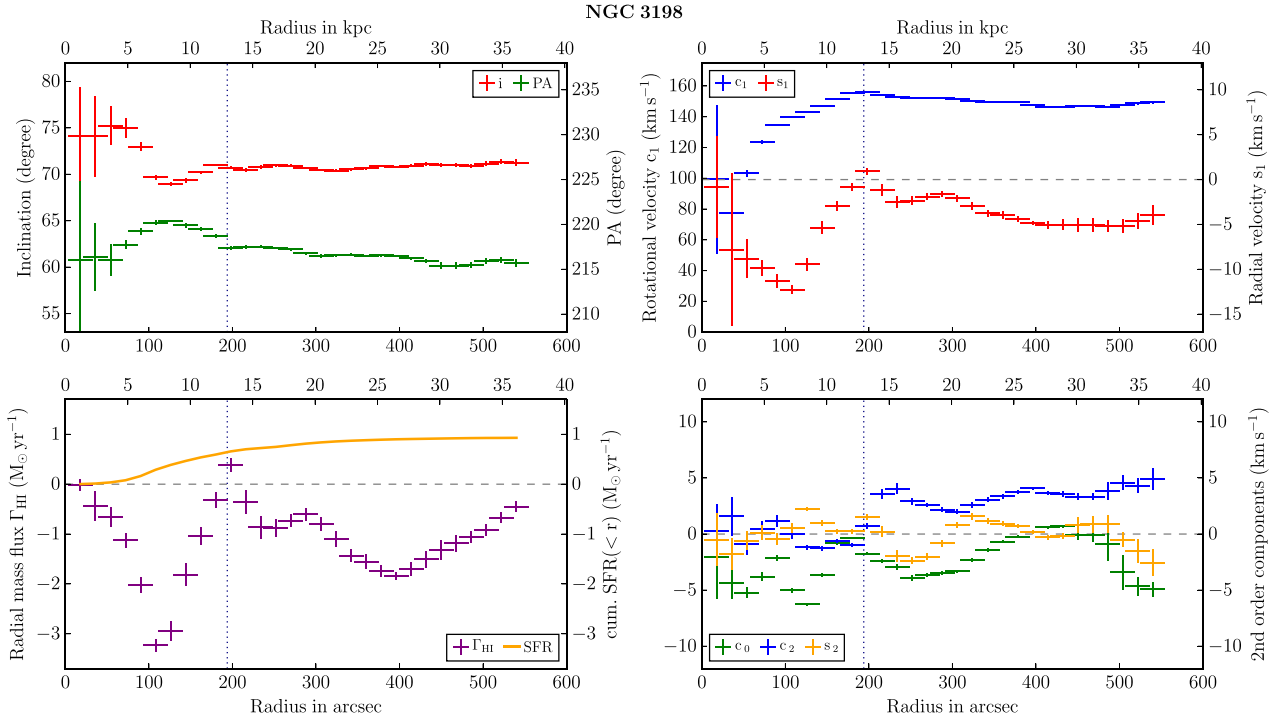


**Figure 13.** The results for NGC 3198 show a flat and smooth disc with some inflow of nearly constant velocity in the outer half of the galaxy.

term should represent a strong lopsidedness of the radial velocity or a significant change of the systemic velocity with radius. Since the latter seems unreasonable, we conclude that this term represents lopsidedness. This in consequence would imply a strong east-west

gradient in the radial velocity field. Gas then would enter the galaxy on the western side with roughly  $30 \text{ km s}^{-1}$ , cross the disc and leave again on the eastern side, which altogether seem quite an unlikely scenario too.

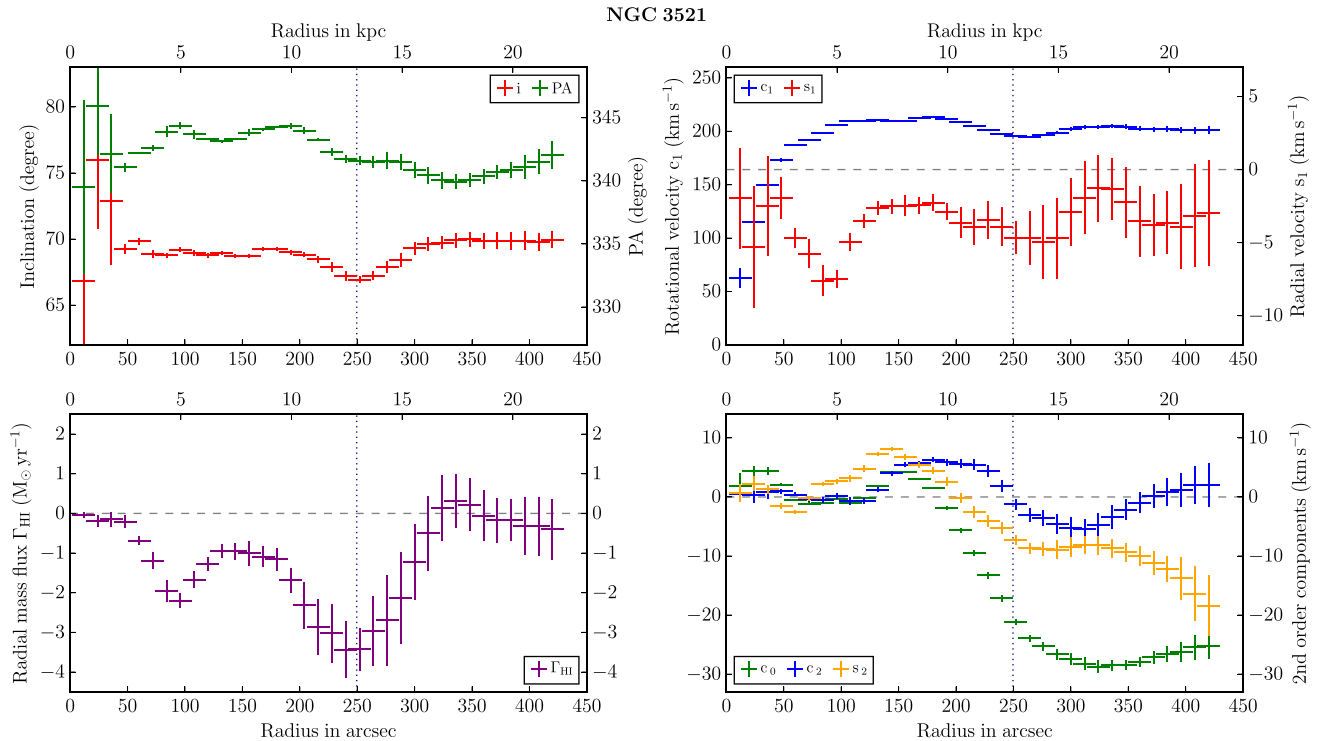


**Figure 14.** The disc geometry of NGC 3521 seems quite flat with some radial inflow mostly at intermediate radii. An odd feature is the  $c_0$  component which drops to a value of  $-30 \text{ km s}^{-1}$  outside of 200 arcsec. This indicates an extreme lopsidedness or hints at other peculiarities in the velocity field. For NGC 3521, no *GALEX* FUV image was available to derive an SFR profile.

However, the overall galaxy appearance is indeed quite asymmetric. Images at optical wavelength show numerous well-pronounced dust lanes and a very extended north-west spiral arm. This arm is also visible in the 21 cm line as extension of the disc. In addition, also a south-east lobe exists which is even more extended. It shows very high fit residuals of up to  $+60 \text{ km s}^{-1}$ . This relatively localised feature introduces the peculiar  $c_0$  values to our fit. We know that NGC 3521 underwent extensive merger activity in the past. Martinez-Delgado et al. (2010) present deep surface photometry which shows several stellar streams and an extended envelope of stars around the galaxy. Also, de Blok et al. (2008) found that a substantial amount of gas is not moving within the plane of the galaxy. This clearly affects our fit.

Given the complex dynamic structure of NGC 3521 and its recent merger history, the results of our fitting procedure need to be considered with caution. The derived fluxes need not necessarily be interpreted as large-scale inward mass motion. Deciphering the kinematics of such a disturbed system most likely is beyond the capabilities of the method, as it relies on the assumption of a relatively unperturbed disc with only mildly varying geometry.

## 5.6 NGC 3621

The analysis for NGC 3621 reveals a relatively simple disc with fairly constant inclination and position angle. This is somewhat surprising, because the galaxy is looking clumpy and inhomogeneous in the integrated intensity map. The visual impression could be influenced by the fact that an extra gas component in the form of a stream or a warp in the line of sight crosses the main disc and creates some foreground confusion (de Blok et al. 2008). The galaxy rotates clockwise and the rotation curve is completely flat outside of 200 arcsec (Fig. 15). The measured radial velocity is of

low amplitude and varies in the range of  $\pm 5 \text{ km s}^{-1}$ . Walter et al. (2008) report a high SFR of  $2 \text{ M}_{\odot} \text{ yr}^{-1}$ . Our coarse SFR estimate from *GALEX* FUV images is substantially lower ( $0.5 \text{ M}_{\odot} \text{ yr}^{-1}$ ) but as mentioned, our aim is to reproduce the radial distribution not the galaxy-integrated amplitude of the star formation activity. Fig. 15 therefore shows the profile we measure scaled to the total SFR reported by Walter et al. (2008). Some slight correlations between the radial H I flow and the SFR profile might be visible, in particular at 100 arcsec where a substantial amount of the star formation takes place and the low-level inflow we measure decreases. However, we do not find signs of large-scale inflow and the recent star formation in NGC 3621 seems to consume the existing gas inventory of the galaxy and is at the moment not fuelled from outside in substantial amounts.

## 5.7 NGC 5055

NGC 5055 exhibits a very complex disc geometry, as indicated in Fig. 16. The southern part of the disc is closer to Earth and rotation occurs in a clockwise direction. In the integrated H I map as shown by Walter et al. (2008), one can clearly distinguish between an inner star-forming part of the galaxy [SFR given by Leroy et al. (2008) is  $2.1 \text{ M}_{\odot} \text{ yr}^{-1}$ , for the radial distribution, compare to Fig. 16] and an outer diffuse ring with a noticeably different inclination angle. The kinematic analysis yields an inclination which first rises to above  $65^\circ$  at 380 arcsec, then declines to  $50^\circ$  at 650 arcsec and then rises again to slightly below  $60^\circ$ . The position angle also changes. The most significant feature is a steep rise by  $30^\circ$  between 500 and 800 arcsec. For the radial velocity, we find values around zero up to a radius of 600 arcsec. Outside of this, in the region of the H I ring, it rises to  $20 \text{ km s}^{-1}$  and declines again towards the outermost part of the galaxy. This corresponds to an outward peak mass flow

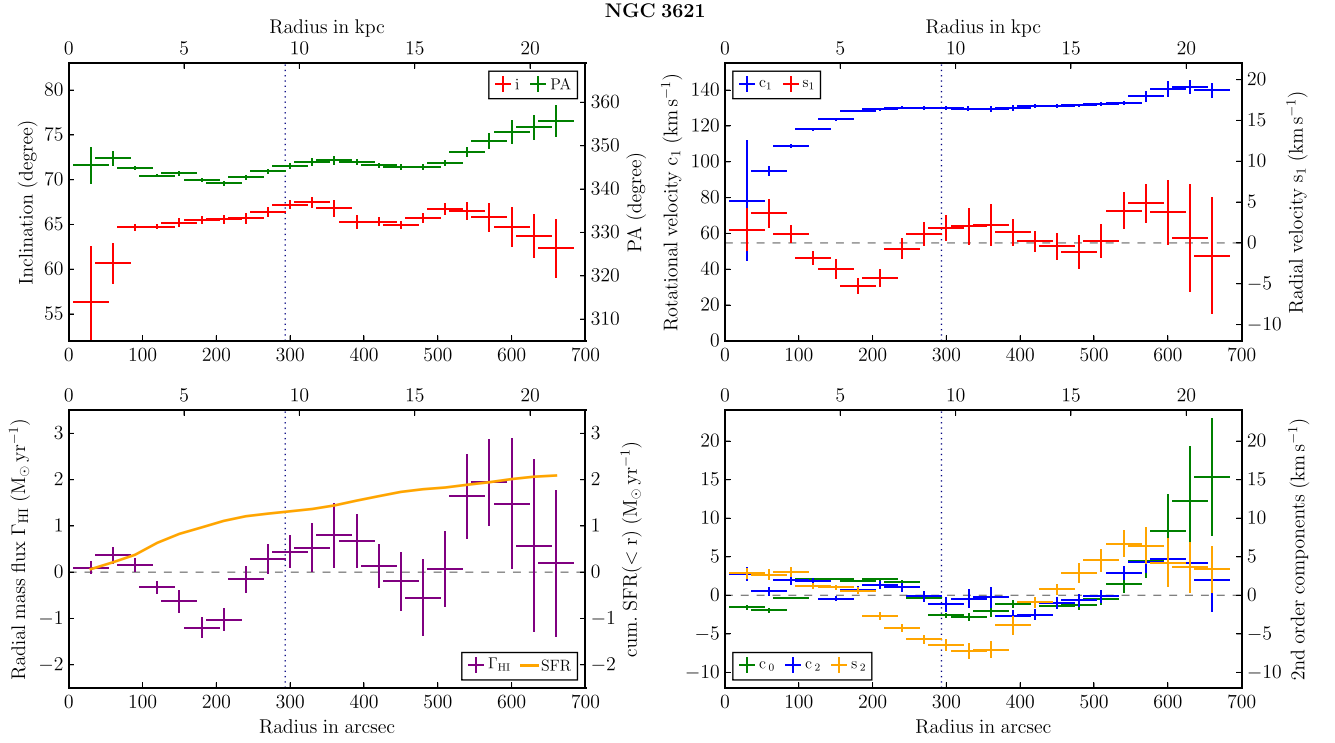


**Figure 15.** Fit results for NGC 3621. The disc is flat, as is the rotation curve. The radial velocity wiggles around zero without clear signs of significant radial motions.

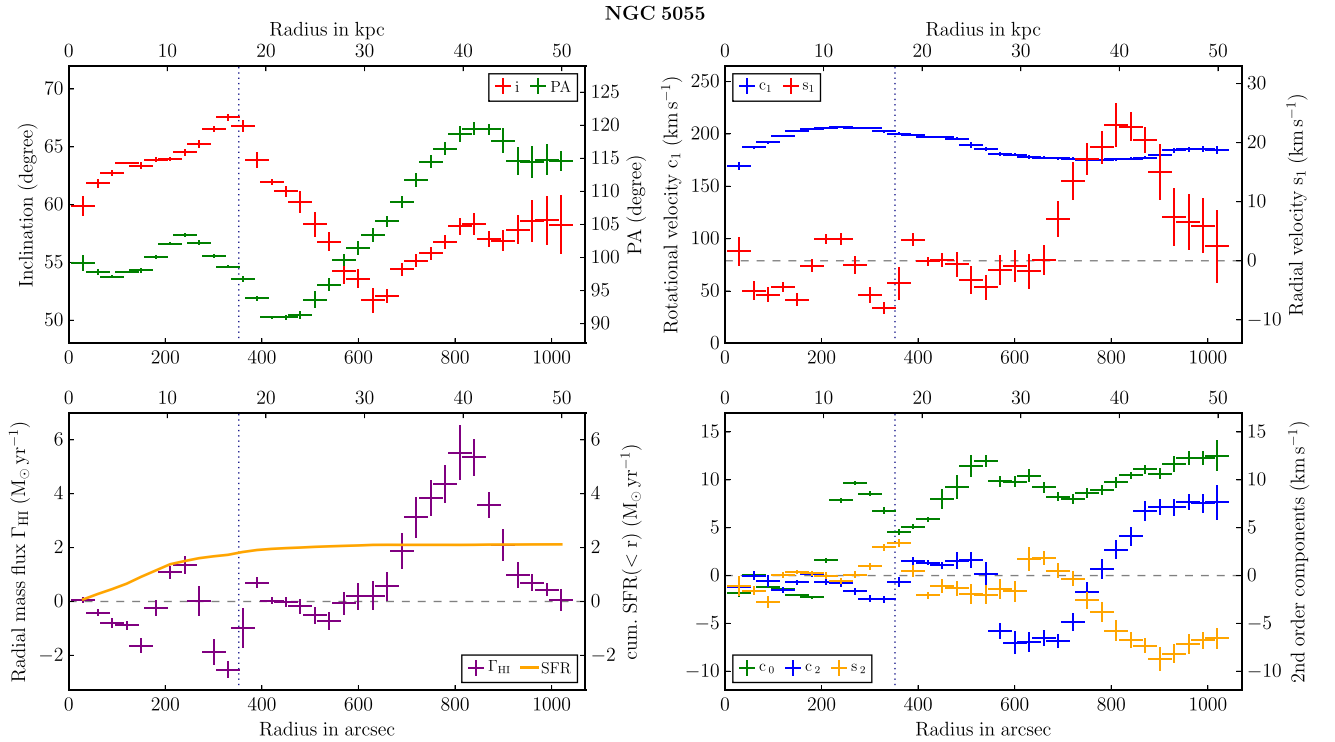


**Figure 16.** Disc geometry and Fourier parameters of NGC 5055. The geometry of the disc shows significant structure compared to the other galaxies in our sample. None of the analysed galaxies shows as much change in inclination and position angle as NGC 5055. We speculate that this is due to an interaction with a dwarf galaxy. A corresponding stellar stream reported by Chonis et al. (2011) intersects the disc at a radius of roughly 600 arcsec. This coincides with the radius at which we see a distinct minimum of the inclination and a strong change of position angle. Inside of 600 arcsec, we find no significant radial motions, further out we find gas moving outwards, peaking at a radius of 800 arcsec and H I mass flow rates of up to  $6 M_{\odot} \text{ yr}^{-1}$ .

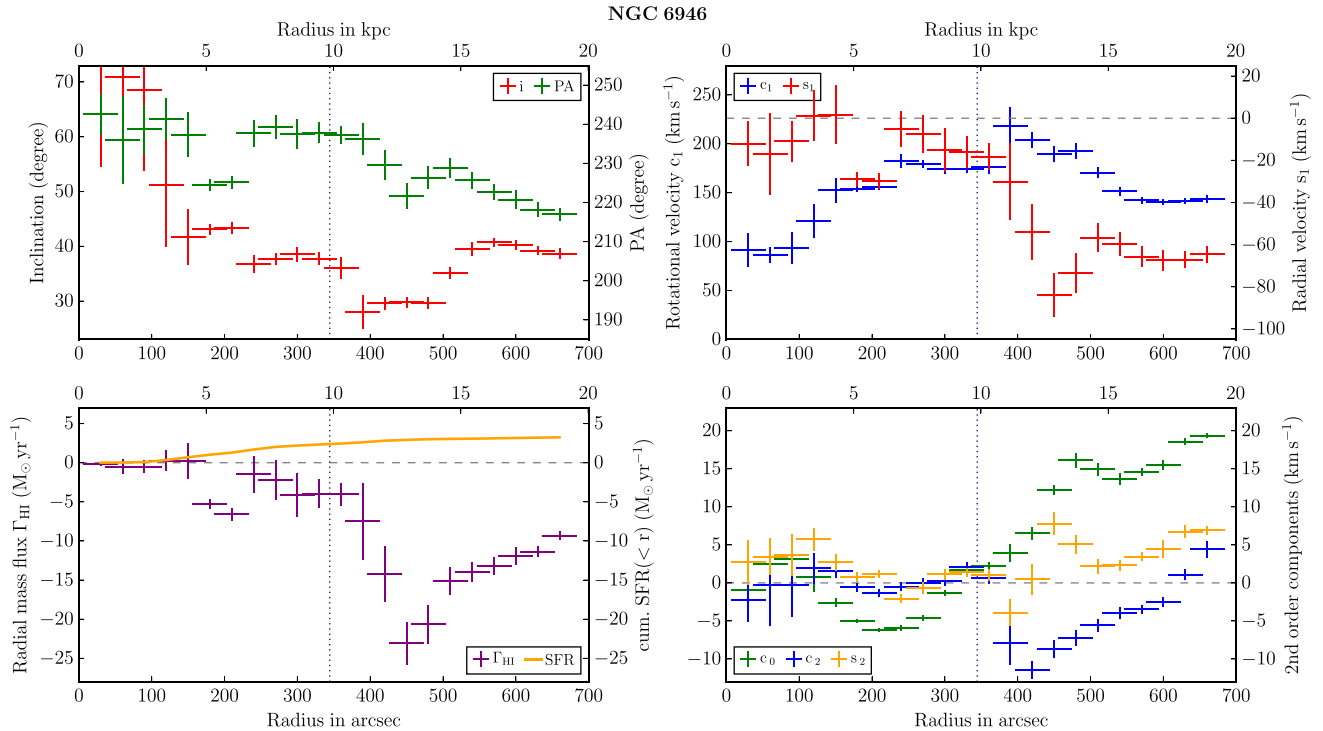


**Figure 17.** Results of the analysis for NGC 6946. The galaxy has a low inclination of about  $35^\circ$  which makes a kinematic analysis difficult and leads to large uncertainties. The determined radial velocity of  $\approx 60 \text{ km s}^{-1}$  translates into an  $\text{H I}$  inflow of  $15 \text{ M}_\odot \text{ yr}^{-1}$ . While this represents an extreme mass flow, NGC 6946 has a high SFR of  $3.2 \text{ M}_\odot \text{ yr}^{-1}$  and a high and extended molecular gas content.

of  $6 \text{ M}_\odot \text{ yr}^{-1}$ . Inside of 600 arcsec, no significant mass flow is detected. The asymmetry terms show quite high and varying values.

Even if the rise of inclination outside of 600 arcsec is quite steep, it is only about 50 per cent of the critical change rate given in equation (15). Therefore, the measured  $s_1$  term should be robust and we consider the  $\text{H I}$  mass flow to be real. From dust lanes we can infer that the galaxy rotates clockwise and the radial flow is directed outwards. Chonis et al. (2011) report the detection of a stellar stream in the outskirts of NGC 5055 via deep optical surface photometry. The stream is inclined with respect to the disc, but not associated with any  $\text{H I}$  structure. NGC 5055 is part of the M51 group and accompanied by dwarf galaxies (Battaglia et al. 2006). The detection of the stream is clear evidence for a recent merger event. From the geometry of the stream presented by Chonis et al. (2011), one could estimate that it passed through the disc of NGC 5055 at a radius of roughly 600 arcsec. This matches strikingly well with the minimum of the inclination, and it is also well within the regime of the steep change in position angle. It seems that the merger has perturbed the disc of NGC 5055 and left an imprint in the  $\text{H I}$  kinematics. Even if the exact dynamics are unknown, it is very likely that the complex disc geometry we find is the direct result of this recent merger event.

There is also a dark dust filament visible in front of the southern half of the stellar disc. It has a quite luminous  $\text{H I}$  counterpart which is easy to identify in the integrated intensity map. From the visual impression of the velocity map, the filament seems to move out of the galactic plane and at a different orbital velocity than the rest of the disc. This probably causes the bump in the inclination at around 350 arcsec since the fit cannot differentiate between the disc velocity and the motion of the filament and fits an average along the line of sight.

## 5.8 NGC 6946

For NGC 6946 we derive a fairly low inclination of  $\sim 35^\circ$  with substantial scatter from ring to ring. Similar results are reported by de Blok et al. (2008). The low and varying inclination makes the fit quite uncertain since the majority of parameters are scaled by  $\sin(i)$ . The fit only converges if we choose quite wide rings (increase in 30 arcsec steps) and we consider it quite likely that the actual uncertainties are larger than the formal error bars shown in Fig. 17.

We determine a moderately varying PA and clockwise rotation and find the nearside of the disc to be the north-west part. The inward radial velocities are very high and in excess of  $-60 \text{ km s}^{-1}$ , which is roughly one third of the rotational velocity. Also, the radial velocity field shows a quite substantial lopsidedness with a difference between north-west and south-east edge of around  $30 \text{ km s}^{-1}$ . Even if we do not take the two rings at 450 and 480 arcsec into account, NGC 6946 shows an extremely high  $\text{H I}$  mass inflow of  $10\text{--}15 \text{ M}_\odot \text{ yr}^{-1}$  in the range from 400 to 650 arcsec. Our fit results are stable and the residuals show no obvious feature that would indicate problems with the fit beyond the large statistical errors. Nevertheless, we express some concern that the derived magnitude of the inflow could be larger than what is physically reasonable and may be exaggerated due to the low inclination of the galaxy.

However, NGC 6946 does exhibit exceptional properties. The SFR is relatively large with a value of  $3.3 \text{ M}_\odot \text{ yr}^{-1}$  (Leroy et al. 2008). The gas-to-stellar mass ratio is also high. For the atomic gas, a value of 20 per cent is reported. For the molecular gas, the number is 12 per cent, which is the largest value in the entire THINGS sample. From the *GALEX* FUV images, we find that a substantial part of the total star formation takes place inside of  $r_{25}$ , well inside the region where we detect the large inflows. The amplitudes of



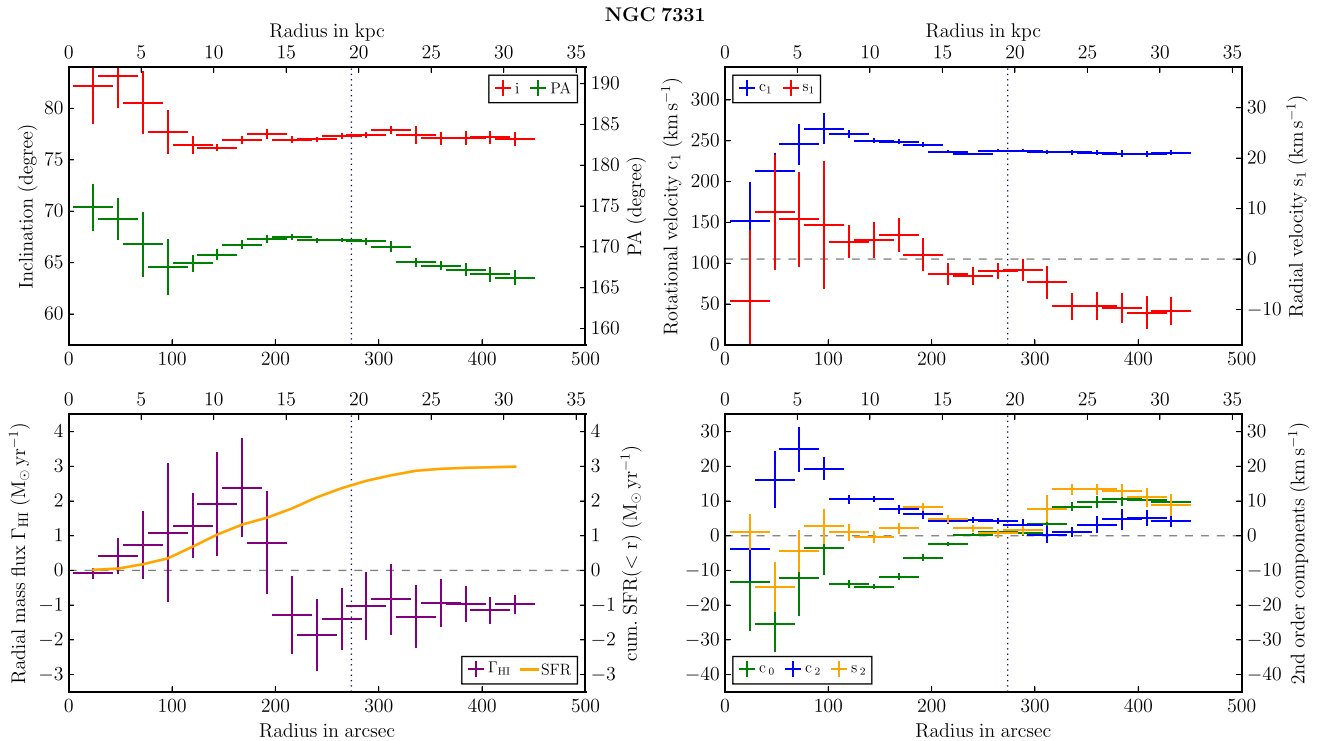


**Figure 18.** Disc geometry and Fourier parameter for NGC 7331. The disc is flat and outside of 300 arcsec we find  $10 \text{ km s}^{-1}$  inflow. Due to the relatively low H I density, this translates into an H I mass flux of only  $1 \text{ M}_{\odot} \text{ yr}^{-1}$ .

inflow and SFR roughly match; however, the uncertainty in the inflow measurements prohibits a detailed comparison.

The general picture we get for NGC 6946 fits the simulations by Marinacci et al. (2014) very well. They ran eight cosmological hydrodynamical zoom simulations of Milky Way-sized haloes using the moving mesh code AREPO to study the evolution of disc galaxies.

They usually find quite fast inflow with radial velocities nearly matching the circular velocity in the outer part of the disc. The gas in the simulated discs is supported by rotation only up to the edge of the luminous disc and outside of this it is highly sub-Keplerian. Although these high radial velocities fit qualitatively to our findings for NGC 6946, their simulations generally predict too small H I discs compared to other spiral galaxies. The authors explain that their objects include far less gas than would be realistic, and we assume that this could affect the size and dynamics of the simulated gas discs.

If the magnitude of the derived inflow is indeed correct, the inflow rates would be uniquely high in our sample. However, given the low inclination of NGC 6946 and the large ring-to-ring variations in the fit, we may expect these inflow rates to be upper limits and presumably should not be taken at face value.

## 5.9 NGC 7331

NGC 7331 is rotating clockwise and the western part of the disc is closer to Earth. Our analysis yields a fairly constant inclination and position angle as well as rotation velocity (Fig. 18). We find some inflow of H I at the level of  $1 \text{ M}_{\odot} \text{ yr}^{-1}$  outside of  $r_{25}$  and outflow inside of it. The radial velocity is close to zero in the inner part and negative at around  $-10 \text{ km s}^{-1}$  in the outer part of the disc. The asymmetry terms are of similar magnitude. In the reconstructed radial velocity field, one sees that inflow predominantly happens

in the northern part of the galaxy. In the southern half, the radial velocity does not substantially deviate from zero. The integrated H I map shows a fairly extended lobe on the northern end of the galaxy and a small one on the south. One possible explanation could be that a relatively localized gas stream flows inwards from the circumgalactic medium and reaches the northern part of the galaxy. Unfortunately, the high inclination of NGC 7331 makes it difficult to study the structure of the northern lobe in more detail, and the observations are not sensitive enough to trace the H I gas further out.

The Leroy SFR for NGC 7331 is nearly as high as for NGC 6946, but the measured H I inflow rate of about  $1 \text{ M}_{\odot} \text{ yr}^{-1}$  is more than an order of magnitude lower. However, all star formation takes place inside of 25 kpc (compare to Fig. 18) and we find basically constant inflow outside of 15 kpc. Despite the mismatch in amplitude, this gives a roughly consistent picture of mass transport and star formation.

## 5.10 NGC 925

For NGC 925, we find that the galaxy is most likely rotating clockwise and that the northern part of the disc is closest to us. There is a nearly linear drop of inclination from above  $85^{\circ}$  in the centre to  $50^{\circ}$  in the outskirts. At the same time the rotation velocity shows a nearly linear rise out to 250 arcsec and then saturates at  $\sim 110 \text{ km s}^{-1}$  (Fig. 19). Optical images clearly show a bar in the galaxy centre. As described in Section 3.2, solid-body rotation makes it impossible to disentangle inclination and rotation, and therefore the inferred disc geometry inside of 250 arcsec may be incorrect. Outside of this radius, however, our fit results should be robust.

The amplitude of the radial velocity is quite high. Outside of 300 arcsec, it rises to a maximum of  $20 \text{ km s}^{-1}$ . This results in an H I outflow of nearly  $5 \text{ M}_{\odot} \text{ yr}^{-1}$  at around 300 arcsec. The integrated

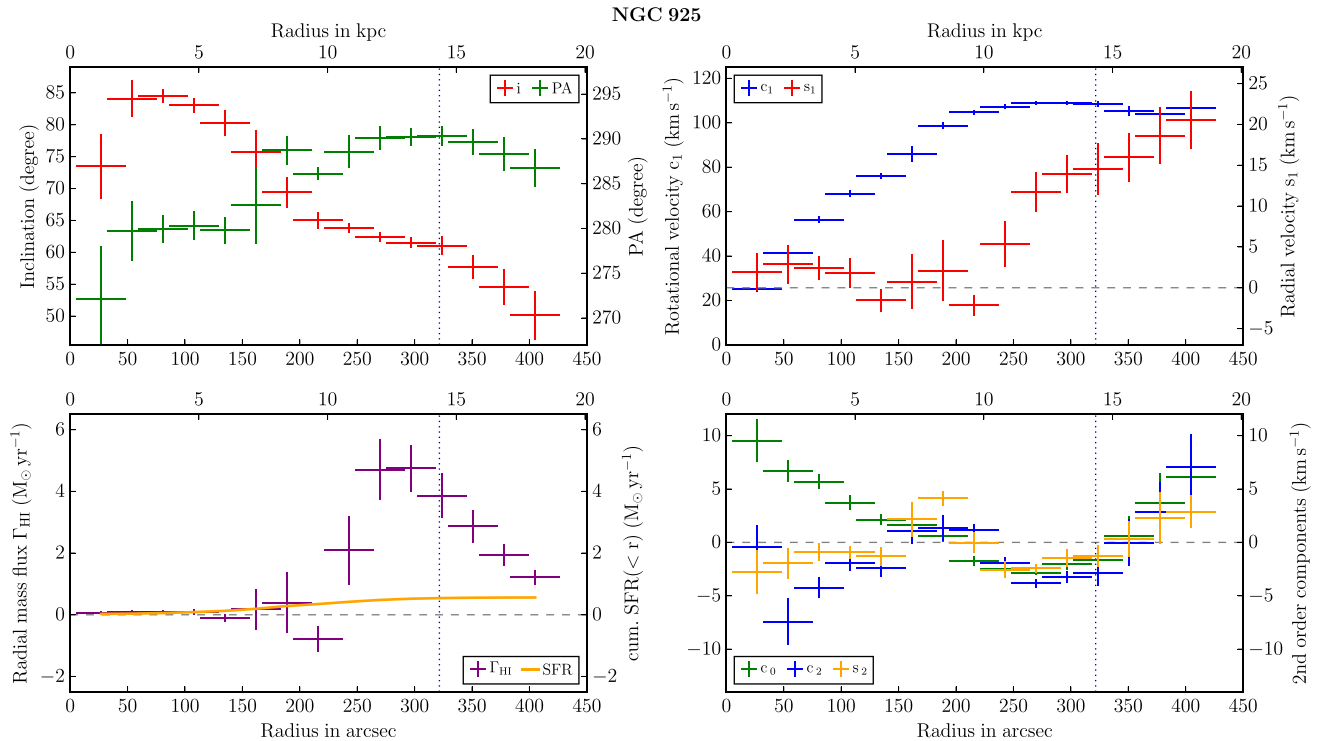


**Figure 19.** The results for NGC 925 indicate a linearly rising rotation curve which complicates the proper determination of the inclination in the inner half of the H I disc (see the discussion in Section 3.2). Outside of 200 arcsec our analysis indicates strong outflows.

H I map clearly shows two extended spiral arms, probably related to interactions or accretion events. Heald et al. (2011) report the detection of an extended H I envelope with complicated streams caused by a minor merger in the Hydrogen Accretion in LOcal GALaxieS survey. They even find a very faint optical counterpart which could be the remnant of a gas-rich dwarf galaxy that was accreted by NGC 925. The fact that we derive outward instead of inward motion is surprising, but the overall picture slightly resembles that of NGC 2841 (Section 5.2).

## 6 CONCLUSIONS

In this kinematic study, we analysed the H I velocity field of 10 disc galaxies from the THINGS survey and investigated the presence of radial inflows, which might supply the star-forming regions in the inner parts with fresh gas and thereby allow continued star formation.

Given that the gas depletion time-scale in most spiral galaxies is short and of the order of  $\sim 2$  Gyr, it is a long-standing problem of galaxy evolution to explain how star formation activity is sustained over cosmological time-scales. If we discard the possibility that most galaxies are observed on the verge of running out of gas, then they must be continuously fed by fresh material. Our aim is to search for signatures of this process.

We started our investigation of the dynamics of H I gas in nearby disc galaxies with the analysis of existing tilted ring fitting methods and the assessment of their statistical reliability. We found that most two-step fitting schemes are unable to recover the full radial inflow in the velocity field and as a consequence developed a new Fourier decomposition scheme that includes second-order terms of rotational and radial velocity and simultaneously determines the position angle and inclination angle as functions of radius. By applying it to mock velocity data, we demonstrated that the new method is

more stable and less susceptible to systematic errors. It is well suited to reliably detect radial flows of material through the disc for galaxies that show no strong warps and no sudden changes of position angle. The method works well for galaxies with intermediate inclination angles and smooth and unperturbed discs, but gives less reliable results for galaxies with complicated kinematics and geometries, for instance if they have recently gone through a merger event that disturbed the disc.

We find clear evidence for radial inflow in NGC 2403 with an amplitude of  $15 \text{ km s}^{-1}$  corresponding to an H I mass flow rate of  $3 \text{ M}_{\odot} \text{ yr}^{-1}$ . Substantial inward mass flux through the outer disc is also detected in NGC 3198 with values up to  $2 \text{ M}_{\odot} \text{ yr}^{-1}$ , and to a lower degree in NGC 2903 and NGC 7331 with values around and below  $1 \text{ M}_{\odot} \text{ yr}^{-1}$ . For NGC 6946, we infer a surprisingly large inflow rate of  $15 \text{ M}_{\odot} \text{ yr}^{-1}$ , but this measurement is affected by the low inclination of the galaxy and is likely to be overestimated.

We compare our radial mass flux profiles to SFR profiles based on GALEX FUV imaging and to SFR measurements from the literature. We find that the rate at which gas gets transported through the disc is sufficient to explain the current star formation activity and if this is indeed representative of the long-term average, then the accretion of new material on to the outer disc of these galaxies and its subsequent inward transport through the disc is sufficient to maintain a steady state over secular time-scales.

However, a detailed comparison of the radial distribution of star formation and mass inflow usually deviates substantially from the naive assumption of a stationary state with a one-to-one relation between inflow and star formation across galaxy discs. This is indicative of additional mass transport processes acting within the galaxies, for example gas ejection by stellar winds, often referred to as galactic fountains.

For NGC 5055 as well as for NGC 2841 and NGC 925, we find that H I gas flows outwards in the outer disc. In NGC 5055, there

is evidence of a recent encounter with a dwarf galaxy. We think that this is the cause for its perturbed disc geometry, and speculate that the angular momentum delivered to the disc by this encounter drives the inferred outward motion. Indications of a recent merger with a gas-rich dwarf galaxy are also reported for NGC 925. We therefore consider the encounter with a dwarf galaxy as a possible explanation for the peculiar properties of all three objects.

Nearly all the galaxies in our sample show some degree of asymmetry like lobes, streams or other types of disc perturbations. Complex kinematic structures thus appear quite common among large spiral galaxies and unperturbed discs are likely to be an exception. To properly model the velocity fields of the observed H I discs, in particular of their outer regions, where these perturbations seem more pronounced, the employed fitting has to be able to adapt to these asymmetries. It would therefore be highly desirable to include as many Fourier components as possible in the simultaneous fit of the H I velocity field, which is a difficult task: the components of the Fourier decomposition of the field are highly degenerate and going beyond the second order is not practical. Clearly, more sensitive observations that cover larger areas especially of the out disc will help to improve our ability to study the H I velocity field; however, the general limitations of the purely kinematic analysis method remain. Doing full justice to the complex velocity patterns observed in these disc galaxies remains a challenging task.

We conclude that there are indeed radial inflows in the discs of galaxies present which can easily be of sufficient magnitude to sustain star formation in the inner parts of galactic discs. However, the situation appears more complex than simply linking the inferred inflow rates to measured SFRs: the inflow rates are often up to an order of magnitude larger than the SFR (to some degree a detection bias, since an inflow rate corresponding to the average SFR of  $\approx 1 \text{ M}_\odot \text{ yr}^{-1}$  in our sample would only be barely detectable with our method) and in every case highly variable throughout the disc. There are a variety of possible explanations like episodic gas accretion, probably related to minor merger events, accretion directly to intermediate radii of the discs or a substantial contribution from internal cycling of gas suggested by the galactic fountain picture. Without dedicated simulations aiming at a precise modelling of gas kinematics including physical feedback schemes, it will probably be impossible to decide in favour of a particular model. While our study based on kinematic data alone could show the existence of radial inflows in disc galaxies, any further investigation will probably not only need superior (deep, extended and good resolution) observational data but also a much broader approach supported by simulations.

## ACKNOWLEDGEMENTS

We thank Milan den Heijer, Juergen Kerp and Shahram Faridani for supplying Effelsberg single-dish data and stimulating discussions. This work made extensive use of the The HI Nearby Galaxy Survey (THINGS) data base (Walter et al. 2008), as well as the NASA/IPAC Extragalactic Database (NED), which is operated by the Jet Propulsion Laboratory, California Institute of Technology, under contract with the National Aeronautics and Space Administration. FB acknowledges support from DFG grant BI 1546/1-1. RSK thanks the Deutsche Forschungsgemeinschaft (DFG) for funding via the SFB 881 *The Milky Way System* (subprojects B1, B2 and B8) as well as via the SPP 1573 *The Physics of the Interstellar Medium*. RSK furthermore acknowledges support from the European Research Council under the European Community's Seventh Framework Programme (FP7/2007-2013) via the ERC Advanced

Grant STARLIGHT (project number 339177). WJGdB was supported by the European Commission (grant FP7-PEOPLE-2012-CIG #333939).

## REFERENCES

- Adams S. M., Kochanek C. S., Beacom J. F., Vagins M. R., Stanek K. Z., 2013, *ApJ*, 778, 164
- Agertz O., Teyssier R., Moore B., 2009, *MNRAS*, 397, L64
- Battaglia G., Fraternali F., Oosterloo T., Sancisi R., 2006, *A&A*, 447, 49
- Begeman K. G., 1987, PhD thesis, Kapteyn Institute, Univ. Groningen
- Bigiel F., Leroy A., Walter F., Brinks E., de Blok W. J. G., Madore B., Thornley M. D., 2008, *AJ*, 136, 2846
- Bigiel F., Leroy A., Walter F., Blitz L., Brinks E., de Blok W. J. G., Madore B., 2010a, *AJ*, 140, 1194
- Bigiel F., Leroy A. K., Seibert M., Walter F., Blitz L., Thilker D., Madore B., 2010b, *ApJ*, 720, L31
- Bigiel F. et al., 2011, *ApJ*, 730, L13
- Binney J., Dehnen W., Bertelli G., 2000, *MNRAS*, 318, 658
- Bird S., Vogelsberger M., Sijacki D., Zaldarriaga M., Springel V., 2013, *MNRAS*, 429, 3341
- Bosma A., 1978, PhD thesis, Univ. Groningen
- Bournaud F., Combes F., Jog C. J., Puerari I., 2005, *A&A*, 438, 507
- Brandt J. C., 1960, *ApJ*, 131, 293
- Bregman J. N., 1980, *ApJ*, 236, 577
- Ceverino D., Dekel A., Bournaud F., 2010, *MNRAS*, 404, 2151
- Chiappini C., Renda A., Matteucci F., 2002, *A&A*, 395, 789
- Chonis T. S., Martinez-Delgado D., Gabany R. J., Majewski S. R., Hill G. J., Gralak R., Trujillo I., 2011, *AJ*, 142, 166
- Daddi E. et al., 2010, *ApJ*, 713, 686
- de Blok W. J. G., Walter F., Brinks E., Trachternach C., Oh S.-H., Kennicutt R. C., 2008, *AJ*, 136, 2648
- Dekel A. et al., 2009, *Nature*, 457, 451
- Ferrière K. M., 2001, *Rev. Mod. Phys.*, 73, 1031
- Fraternali F., Binney J. J., 2006, *MNRAS*, 366, 449
- Fraternali F., Binney J. J., 2008, *MNRAS*, 386, 935
- Fraternali F., van Moorsel G., Sancisi R., Oosterloo T., 2002, *AJ*, 123, 3124
- Fraternali F., Oosterloo T. A., Sancisi R., Swaters R., 2005, in Braun R., ed., *ASP Conf. Ser. Vol. 331, Extra-Planar Gas. Astron. Soc. Pac.*, San Francisco, p. 239
- Genzel R. et al., 2010, *MNRAS*, 407, 2091
- Heald G. et al., 2011, *A&A*, 526, 118
- Hopkins A. M., McClure-Griffiths N. M., Gaensler B. M., 2008, *ApJ*, 682, L13
- Jiang L., Binney J., 1999, *MNRAS*, 303, L7
- Kalberla P. M. W., 2003, *ApJ*, 588, 805
- Kerp J., Winkel B., Ben Bekhti N., Flöer L., Kalberla P. M. W., 2011, *Astron. Nachr.*, 332, 637
- Klessen R. S., Hennebelle P., 2010, *A&A*, 520, A17
- Kornreich D. A., Lovelace R. V. E., Haynes M. P., 2002, *ApJ*, 580, 705
- Kuzio de Naray R., Arsenault C. A., Spekkens K., Sellwood J. A., McDonald M. D., Simon J. D., Teuben P., 2012, *MNRAS*, 427, 2523
- Leroy A. K., Walter F., Brinks E., Bigiel F., de Blok W. J. G., Madore B., Thornley M. D., 2008, *AJ*, 136, 2782
- Leroy A. K. et al., 2009, *AJ*, 137, 4670
- Leroy A. K. et al., 2013, *AJ*, 146, 19
- Linsky J. L., 2003, *Space Sci. Rev.*, 106, 49
- Lubowich D. A., Pasachoff J. M., Balonek T. J., Millar T. J., Tremonti C., Roberts H., Galloway R. P., 2000, *Nature*, 405, 1025
- Mac Low M.-M., Klessen R. S., 2004, *Rev. Mod. Phys.*, 76, 125
- Marinacci F., Pakmor R., Springel V., 2014, *MNRAS*, 437, 1750
- Martinez-Delgado D. et al., 2010, *AJ*, 140, 962
- Meidt S. E. et al., 2013, *AJ*, 779, 45
- Miller E. D., Bregman J. N., Wakker B. P., 2009, *ApJ*, 692, 470
- Naab T., Ostriker J. P., 2006, *MNRAS*, 366, 899
- Ostriker E. C., Binney J. J., 1989, *MNRAS*, 237, 785
- Ostriker J. P., Tinsley B. M., 1975, *ApJ*, 201, L51

- Peek J. E. G., 2009, *ApJ*, 698, 1429  
Pflamm-Altenburg J., Kroupa P., 2009, *ApJ*, 706, 516  
Popping G., Perez I., Zurita A., 2010, *A&A*, 521, 13  
Prochaska J. X., Wolfe A. M., 2009, *ApJ*, 696, 1543  
Rogstad D. H., Lockhart I. A., Wright M. C. H., 1974, *ApJ*, 193, 309  
Saintonge A. et al., 2011, *MNRAS*, 415, 61  
Saintonge A. et al., 2012, *ApJ*, 758, 73  
Salim S. et al., 2007, *ApJ*, 173, 267  
Sancisi R., Fraternali F., Oosterloo T., van der Hulst T., 2008, *A&AR*, 15, 189  
Schlafly E., Finkbeiner D. P., 2011, *ApJ*, 737, 103  
Schoenmakers R. H. M., Franx M., de Zeeuw P. T., 1997, *MNRAS*, 292, 349  
Sellwood J. A., Sanchez R. Z., 2010, *MNRAS*, 404, 1733  
Sellwood J. A., Spekkens K., 2015, preprint ([arXiv:1509.07120](https://arxiv.org/abs/1509.07120))  
Shapiro P. R., Field G. B., 1976, *ApJ*, 205, 762  
Shetty R., Kelly B. C., Bigiel F., 2013, *MNRAS*, 430, 288  
Shetty R., Kelly B. C., Rahman N., Bigiel F., Bolatto A. D., Clark P. C., Klessen R. S., Konstantin L. K., 2014a, *MNRAS*, 437, L61  
Shetty R., Clark P. C., Klessen R. S., 2014b, *MNRAS*, 442, 2208  
Spekkens K., Sellwood J. A., 2007, *ApJ*, 664, 204  
Trachternach C., de Blok W. J. G., Walter F., Brinks E., Kennicutt R. C., Jr, 2008, *AJ*, 136, 2720  
van der Marel R. P., Franx M., 1993, *ApJ*, 407, 525  
van Woerden H., Wakker B. P., 2004, in van Woerden H., Wakker B. P., Schwarz U. J., de Boer K. S., eds, *Astrophysics and Space Science Library*, Vol. 312, High Velocity Clouds. Kluwer, Dordrecht, p. 195  
Walter F., Brinks E., de Blok W. J. G., Bigiel F., Kennicutt R. C., Jr, Thornley M. D., Leroy A., 2008, *AJ*, 136, 2562  
Wong T., Blitz L., Bosma A., 2004, *ApJ*, 605, 183  
Zaritsky D., Rix H., 1997, *ApJ*, 477, 118

This paper has been typeset from a  $\text{\LaTeX}$  file prepared by the author.